DEPARTMENT OF PHYSICS
UNIVERSITY OF JYVÄSKYLÄ
RESEARCH REPORT No. 12/2012

CHARACTERIZATION OF STRUCTURE AND DIFFUSION IN GEOLOGICAL MATERIALS

BY

MIKKO VOUTILAINEN

Academic Dissertation
for the Degree of
Doctor of Philosophy

Jyväskylä, Finland
December 2012

DEPARTMENT OF PHYSICS
UNIVERSITY OF JYVÄSKYLÄ
RESEARCH REPORT No. 12/2012

CHARACTERIZATION OF STRUCTURE AND DIFFUSION IN GEOLOGICAL MATERIALS

BY
MIKKO VOUTILAINEN

Academic Dissertation
for the Degree of
Doctor of Philosophy

To be presented, by permission of the
Faculty of Mathematics and Natural Sciences
of the University of Jyväskylä,
for public examination in Auditorium FYS-1 of the
University of Jyväskylä on December 17th, 2012
at 12 o'clock noon

Jyväskylä, Finland
December 2012

ISBN 978-951-39-9359-7 (PDF)
ISSN 0075-465X

ISBN 978-951-39-4995-2
ISSN 0075-465X

Preface

The work reviewed in this Thesis has been carried out during the years 2006-2012 in the Department of Physics at the University of Jyväskylä. Financial support from the Finnish Research Programme on Nuclear Waste Management (KYT) is gratefully acknowledged.

First of all, I would like to thank Professor Jussi Timonen for his guidance during these years, for possibility to work here in his group, and for his valuable contribution to the preparation of the enclosed articles in Appendices and to this Thesis. Your positive and optimistic attitude has carried over many obstacles. I am grateful for Dr. Marja Siitari-Kauppi for fruitful collaboration during these years. Maikki, it has always been a pleasure to visit Helsinki and I have had a lot of fresh ideas to bring back home. I really look forward to working with you in the future. I want to express my gratitude to Dr. Paul Sardini for guidance in the world of simulations and for valuable collaboration. I am also thankful that I have had an opportunity to spend time with you and your family in France. I would like to thank Dr. Pekka Kekäläinen for mathematical back up, Antero Lindberg for help in geological issues, Dr. Markko Myllys for guidance in tomographic imaging, Tuomas Turpeinen for help with image analysis, Einari Periäinen for technical support, and Esa Rehn and Jani Maaranen for their guidance in the beginning of my Ph.D. work.

Finally, I thank my parents Eila and Esko for their support and understanding. This achievement would not have been possible without you, not only for the obvious reasons. I want also express my gratitude to my brother Jussi, whole family and my friends for the moments spent by rapids, in nature, and on tatami. Most of all, I thank my beloved fiancée Jenni. Our journey together has not yet been as long as this work has taken, but it certainly has been more joyful and it has given me the strength to conclude this Thesis.

Jyväskylä, December 2012

Mikko Voutilainen

Abstract

This work deals with two important factors of the element transport in geological materials. Firstly, element diffusion is an important migration process in geological materials, especially when considering transport next to water conducting fractures and shear zones. Secondly, the structure of the pore network forms an environment for migration of elements to take place. These two factors are important when considering radionuclide transport in geological materials in which all affecting processes are not fully understood yet. Therefore further information and development of analysis methods are needed.

First of all, a semi-analytical solution for advection-matrix diffusion equations in the case of a well-mixed flow past a porous matrix was developed. Solution is based on a Laplace transform of the equation and on using appropriate dimensionless variables. The matrix-diffusion models considered here include the effects of a finite depth of the matrix, varying aperture of the flow channel, the shape of the input pulse, and longitudinal diffusion and Taylor dispersion of the element in the flow channel as well as a non-zero initial element concentration in the matrix.

In order to validate the developed solutions, a measuring system was constructed. Matrix diffusion was illustrated by observing the migration of KCl-tracer in the water flowing through a channel facing a porous matrix. Migration of K^+ and Cl^- ions was monitored by measuring the electrical conductivity of the solution. The experimental system allowed also measurement of the concentration profile inside the porous matrix, but the focus was here on the input and output (breakthrough) curves. The effects of a finite depth of the matrix and non-zero initial concentration of tracer, predicted by semi-analytical solutions, were successfully validated by the experiments.

Secondly, a method to characterize pore network and mineral distribution of geological materials was developed using X-ray micro computed tomography (X-μCT), ^{14}C-labeled-polymethylmethacrylate (^{14}C-PMMA) method, and scanning electron microscopy (SEM). As an example a sample of altered Sievi tonalite was used. X-μCT was used to create 3D density maps of the samples from which different minerals and pores were segmented. From these density maps mineral abundances, porosity, connectivity, porosity distribution and pore size distribution were determined, together with qualitative information about the structure of minerals and pores.

X-μCT offers information only of structures whose size is above the detection limit. In order to get information below this limit, the ^{14}C-PMMA method and SEM were applied. Different minerals in the sample were identified by SEM, after which these minerals were linked to different components observed in the X-μCT images. The

^{14}C-PMMA method gives a 2D porosity map of imaged rock surface in which porosity of each pixel represents the averaged porosity over its area, and thus it offers information even from nanometer scale. Further, this information was used to determine the intragranular porosities by superimposing the 2D porosity map with stained and segmented image of the corresponding rock surface and then averaging the pixel porosities over each mineral. Finally, 3D porosity maps of the samples were constructed by combining intragranular porosities and segmented tomographic images.

Thirdly, these research issues above were combined by modeling diffusion in tomographic images using time domain diffusion (TDD) simulations. The TDD method is a fast particle tracking method which allows to model diffusion in 3D heterogeneous media when local porosities and diffusion coefficients are known. The method was first validated in various cases including comparison to analytical and numerical solution of the diffusion equation. In addition, the results produced by the method were compared to ones by discrete-time random-walk simulations.

TDD simulations were first applied to analyzing a diffusion experiment of tritiated water (HTO) in altered Sievi tonalite and to determine the apparent diffusion coefficient. Then the TDD method was applied to study the effect of material heterogeneity on diffusion processes using a sample of altered Sievi tonalite. This study was done by comparing simulated in-diffusion profiles in samples with heterogeneous and homogeneous distribution of porosity and known diffusion coefficients. In the case of altered Sievi tonalite, inclusion of heterogeneity in the porosity increased the apparent diffusion coefficient by 16%. The method was also found to be suitable when considering the effects of different mineral components and diffusion direction.

Author Mikko Voutilainen
Department of Physics
University of Jyväskylä
Finland

Supervisor Professor Jussi Timonen
Department of Physics
University of Jyväskylä
Finland

Reviewers Dr. Kari Rasilainen
VTT Technical Research Centre of Finland
Finland

Dr. Josep Soler
Department of Geosciences
Institute of Environmental Assessment and Water Research
Barcelona
Spain

Opponent Professor Rainer Salomaa
Department of Applied Physics
Aalto University
Finland

List of Publications

I Voutilainen, M., Lamminmäki, S., Siitari-Kauppi, M., Breitner, D., and Timonen, J.: Physical rock matrix characterization: structural and mineralogical heterogeneities in granite. Mater. Res. Soc. Symp. P. 1124, 1124-Q07-03 (2009)
https://doi.org/10.1557/PROC-1124-Q07-03

II Voutilainen, M., Kekäläinen, P., Hautojärvi, A., and Timonen, J.: Validation of matrix diffusion modeling, Phys. Chem. Earth 35(6-8), 259-264 (2010)
https://doi.org/10.1016/j.pce.2010.04.005

III Kekäläinen, P., Voutilainen, M., Poteri, A., Hölttä, P., Hautojärvi, A., and Timonen, J.: Solutions to and validation of matrix-diffusion models. Transport Porous Med. 87, 125-149 (2011)
https://doi.org/10.1007/s11242-010-9672-y

IV Voutilainen, M., Siitari-Kauppi, M., Sardini, P., and Timonen, J.: Porespace characterization of an altered tonalite by X-ray computed microtomography and the ^{14}C-labeled-polymethylmethacrylate method. J. Geophys. Res. 117, B01201 (2012)
https://doi.org/10.1029/2011JB008622

V Voutilainen, M., Sardini, P., Siitari-Kauppi, M., Kekäläinen, P., Aho, V., Myllys, M., and Timonen, J.: Diffusion of tracer in altered tonalite: experiments and simulations with heterogeneous distribution of porosity. Transport Porous Med. In the print (online version available)
https://doi.org/10.1007/s11242-012-0090-1

The author of this work has contributed to construction and testing of the experimental equipment for matrix diffusion, and carried out these experiments. He wrote the first draft of related article (II) and participated in the analysis of the data as well as in the writing of the related article (III).

The author did all of the tomographic measurements and the related data analysis, and participated in the analysis of results by the other methods used. He wrote the first drafts of the related articles (I, IV) and participated in their finalization.

The author extended the existent TDD method for the present application, and did all the simulations together with the related data analysis. He wrote the first version of article (V) and participated in its finalization.

Contents

Chapter 1

Introduction

Many countries are building or planning to build underground repositories for disposal of the highly radioactive spent nuclear fuel [1, 2, 3]. Crystalline rock has been chosen to be the host medium for the repository in, e.g., Finland and Sweden [4, 5, 6]. The rods of spent nuclear fuel to be placed in the repository will be isolated from the geosphere by several engineered barriers, but as man-made constructions may eventually break, radioactive elements may then be released from canisters into the surrounding geosphere. This may cause migration of radioactive elements, first into the geosphere and eventually to the biosphere, which may pose a threat to water resources and nature. Therefore, it is essential to estimate the sphere of influence for migration of radionuclides in the geosphere. The time perspective of the safety assessments of nuclear waste repositories spans up to several hundreds of thousands of years including at least one glaciation, which makes the durability estimation of repository systems even more complicated [7, 8, 9, 10].

Matrix diffusion and sorption are believed to be the most significant processes that retard the migration of radionuclides in the geosphere [11, 12, 13]. The main migration pathways of radionuclides in the bedrock are formed by water conducting fractures, and the zones composed of them, in which advective transport dominates the migration of radionuclides. However, molecular diffusion allows radionuclides to migrate from the flow into microscopically small pores of the crystalline rock matrix filled by stagnant pore water. The volume of water in the matrix is orders of magnitude larger than the water flowing in the open fractures [14]. Therefore, the concentration of radionuclides will be diluted and migration retarded in the open fractures. In this sense it is essential to know the characteristics of the surrounding rock matrix and analyze carefully its effect on the migration process.

Matrix diffusion has already received notable research interest over the past three

decades [15, 16, 11, 17, 18], and matrix diffusion in crystalline and sedimentary rocks in particular [19, 18, 20, 21]. Also in-situ experiments are being planned and carried out in underground rock laboratories under realistic conditions [22, 23, 24, 25, 26, 27]. However, in situ experiments are rather difficult to interpret because all the factors in the actual migration environment are not known. From this point of view it is essential to determine parameters for in situ experiments and validate transport models under well-controlled laboratory conditions [28, 29, 30, 31, 32]. Typically matrix diffusion problems have been solved by different types of numerical methods with a varying number of possible factors included [33, 34, 35, 36, 37, 38, 39, 40, 41]. However, analytical solutions for simple advection-diffusion systems have only been found in some simplified cases [11]. In practical situations more general solutions are often needed, since they may be applied more effectively, e.g., in safety analysis or performance assessment of nuclear waste repositories. Generally, it would also be advantageous to have an option to include in a single model various different phenomena that may occur in realistic conditions.

The pore structure and structure related properties, e.g. porosity, tortuosity, constrictivity, and specific surface area, of materials strongly affect the diffusion of solutes in them. Earlier studies have shown that higher connectivity and lower tortuosity increase the diffusive migration of elements [42, 43, 44], while lower constrictivity decreases the diffusion coefficient [45, 46, 47]. Small constrictivity applies to the case where the size of pore throats is small compared to that of pores. During the past decades various attempts have been made to find a relationship between structural properties and diffusion coefficients [48, 47, 49]. However, these relationships are usually strongly material and case dependent, and unambiguous relationships have not been found yet. In addition, often in practically relevant cases it is difficult to determine or measure exact values for these parameters [50]. X-ray tomography together with other imaging methods, e.g. scanning electron microscopy (SEM), confocal microscopy, and the ^{14}C-labeled-polymethylmethacrylate (^{14}C-PMMA) method, offer new and valuable tools to study inter-dependence on structural and transport properties. Recent developments of these techniques have made it possible to study smaller structures in larger scale.

First X-ray tomographic devices were developed for medical imaging [51, 52]. In spite of that, it was clear that X-ray tomography had also great potential in materials research. In the research of geological materials X-ray tomography has already proven its applicability [53, 54, 55]. It has been applied in paleontology [56, 57], sedimentology [58, 59], petrology [60, 54], soil science [61, 62], petroleum engineering [63, 64, 65], and fluid flow research [66], for instance, when the 3D structure of the geological material has been of interest. Recent studies have used X-ray micro-computed-tomographic (X-μCT) reconstructions to determine various parameters, such as porosity, pore size distribution, grain size distribution, connectivity, tortuosity, and specific surface area,

which characterize the structure of porous materials [67, 68, 69, 70, 71]. When analyzing submicrometer features of geological samples of reasonable size (up to centimeter scale), the resolution achievable by X-μCT does not, however, allow for a detailed enough analysis. So as to be able to analyze such features, X-μCT could be combined with more accurate 2-D methods of analysis, such as SEM and the ^{14}C-PMMA method. Simultaneous combination of these different techniques has not been attempted very often, although such combinations would be advantageous as a wider range of length scales in the structural features of rock would thus be covered. Previously, SEM has been used in combination with either X-μCT [72] or the ^{14}C-PMMA method [73]. The ^{14}C-PMMA method has been developed to study the porosity, pore structure, and diffusion pathways of granitic rock in centimeter scale samples [74, 75, 76]. Even though the pixel size of the ^{14}C-PMMA method is tens of micrometers, it, nevertheless, offers information at a submicrometer level by averaging the porosity over the pixel area. In the past two decades the ^{14}C-PMMA method has been applied in various studies concerning the pore structure of and diffusion in geological materials [32, 77, 78, 73, 79, 80]. Also SEM has been found to be a valuable tool in geosciences when characterizing the pore structure or identifying different minerals [81, 82, 83, 84].

As stated above, the microscopic structure of materials has a strong effect on the migration of solutes in them. From the point view of nuclear waste management, lack of knowledge of the effect of microscopic heterogeneity on diffusion makes it difficult to extract parameters relevant for the matrix diffusion concepts used in performance assessments. Generally, the effect of heterogeneity on diffusive migration processes is not straightforward. In a microscopic scale heterogeneity of geological materials typically consists of mineral grains and boundaries around them, fractures and pores formed e.g. by hydrothermal alteration. In some cases these fractures and pores may create particular open networks that make migration faster and increase diffusion coefficient [48, 85, 86]. Often these networks compose the majority of the connected porosity of the medium, and dominate diffusive migration in them [49, 87, 32]. However, additional connected porosity in the mineral grains (intragranular or solution porosity) next to grain boundaries, fissures and micro fractures, may also have an important effect on diffusion [17, 88]. Intragranular porosity may increase the diffusion by providing increased connectivity, or decrease it, which is seen especially in the late time behaviour in diffusion experiments. Heterogeneity may also slow down the diffusion if the material contains for example impermeable zones [89, 90].

Previously diffusion problems involving heterogeneous distribution of diffusion coefficient and/or porosity have been simulated using a continuous-time random walker (CTRW) [91, 92], lattice-Boltzmann simulations [93, 94], or more traditional methods [95, 96]. In addition, CTWR methods have been widely used for solving advection-dispersion problems [97] in which matrix diffusion may also be included [98], as well

as when studying anomalous transport including advection in heterogeneous porous materials [99, 100]. In addition, the time domain diffusion (TDD) method has been developed for simulating diffusion in heterogeneous media [101, 102]. Construction of the TDD method has been inspired by and it has been modified from a CTRW method developed to study the permeability and conductivity of heterogeneous materials [103]. The time-domain realization of the random walker is a rapid particle-tracking method that gives an opportunity to simulate diffusion in heterogeneous materials when the local porosities and diffusion coefficients are known. In this method a particle is forced to jump to a neighbouring point during a certain random transition time, which makes it faster than the traditional particle-tracking methods [104]. Transition probabilities and times are proportional to the local porosities and diffusion coefficients [101]. This method has been used before in two-dimensional (2D) systems [104, 105, 79], but increased computing power and advances in tomographic imaging have recently made it possible to introduce the TDD method also for larger samples and in three dimensions (3D) [106].

The main objectives of this Thesis were to develop characterization methods for the pore space of crystalline rock, and analysis methods for tracer diffusion in such materials. In the end motivation was to combine these objectives so as to find a procedure to model diffusion in a realistic description of tight crystalline rock. To this end: 1. A semi-analytical solution for the advection-matrix-diffusion model was derived. One of the solutions was validated by experiments in the case of matrix of finite depth and non-zero initial concentration of the tracer in the porous matrix. 2. Pore structures of geological samples were characterized combining results of X-μCT, the ^{14}C-PMMA method and SEM analyses. As the main outcome a method was developed for creating 3D porosity maps of geological samples. 3. Diffusion in one of the constructed porosity maps was simulated applying the TDD method. In addition, this method was validated in 3D using various situations and a diffusion measurement was performed in order to find the diffusion coefficient for simulations with heterogeneous distribution of porosity. The simulations performed in a sample of heterogeneous rock unite, in some sense, previous research interests. In the structure characterization and diffusion simulations studies altered Sievi tonalite was used as sample material. This choice was motivated by the fact that geology, mineralogy, structure, and diffusive properties of Sievi tonalite have been subjects of various earlier studies [107, 108, 31, 32, 109, 110], and that alteration has rendered its structure well suited for tomographic analysis with the resolution available at present.

Chapter 2

Experimental validation of the matrix diffusion model

In this chapter a model for the transport system in which a pulse of solution including tracer molecules is advected along a flow channel with porous walls is validated. Here an analytical solution in the form of series expansion in the case of a finite depth of the porous wall (matrix) is first presented. The model is then validated using this solution by measuring breakthrough curves by specific laboratory experiments and comparing the measured curves with the ones that follow from the above solution. Other solutions including a matrix of infinite depth, a radioactive tracer, varying aperture of the flow channel, and longitudinal diffusion and Taylor dispersion of the tracer in the flow channel, are found in the article enclosed in Appendix III.

2.1 Mathematical model for matrix diffusion in the case of matrix of finite depth

A situation considered here consists of system in which fluid flows past a porous matrix (porosity ϵ) of finite depth L_z in a channel of length L, height of the aperture $2b$, and width of the aperture h. A schematic layout of the migration system including the flow channel and the porous matrix is shown in Fig. 2.1. Our goal was to determine an analytical expression for the breakthrough curve in the case when the input concentration and the initial concentrations of the tracer in the flow channel and in the porous matrix were all known (but arbitrary). A mathematic model is presented here for this case using a non-radioactive and non-sorbing tracer.

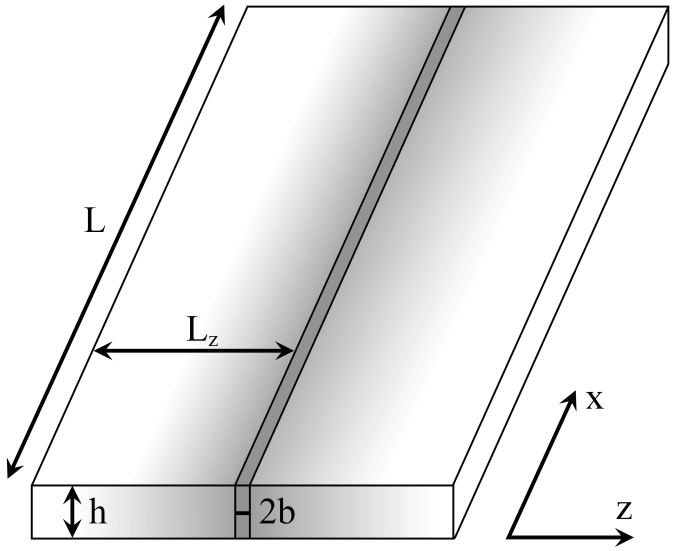

Figure 2.1. *Dimensions and coordinate axes in the model used here for a fracture in a porous medium. Coordinate x is parallel to the flow channel and coordinate z is perpendicular to it, indicating the distance of a point in the porous matrix from the fracture.*

Tracer is assumed to migrate in the flow channel (in the x direction) only by advection and only by diffusion in the porous matrix (in the z direction). In the present case tracer concentrations in the flow channel (C) and porous matrix (C_m) are governed by the equations [11]:

$$\begin{aligned} &\frac{\partial C}{\partial t}(x,t) + v\,\frac{\partial C}{\partial x}(x,t) = \frac{\epsilon\, D_a}{b}\,\frac{\partial C_m}{\partial z}(x,0,t) \\ &\frac{\partial C_m}{\partial t}(x,z,t) - D_a\,\frac{\partial^2 C_m}{\partial z^2}(x,z,t) = 0, \end{aligned} \tag{2.1}$$

where v is the flow velocity in the channel and D_a is the apparent diffusion coefficient of the tracer in the porous matrix. When a conservative tracer is used, D_a is equivalent to the pore diffusion coefficient (D_p) [11]. In the present case the boundary and initial conditions can be expressed in the form:

$$\begin{aligned} &C_m(x,z,0) = C_0(x,z) \qquad C(x,0) = C_0(x,0) \\ &C_m(x,0,t) = C(x,t) \qquad C(0,t) = C_1(t) \\ &\frac{\partial C_m}{\partial z}(x,L_z,t) = 0. \end{aligned} \tag{2.2}$$

Here C_0 is the initial concentration of tracer in the matrix, and C_1 its input concentration. The subject of interest here is concentration at the end of the channel, $C(L,t)$, i.e. the breakthrough curve.

The diffusion equation for $C_m(x,z,t)$, the second line in Eq. 2.1, can be solved by separation of variables, and the solution is a sum of contributions from the tracer coming to the matrix from the flow channel ($C_m^{(1)}$) and from the tracer that is already initially in the matrix ($C_m^{(2)}$):

$$C_m = C_m^{(1)} + C_m^{(2)}. \tag{2.3}$$

The boundary and initial conditions for $C_m^{(1)}$ and $C_m^{(2)}$ are given by

$$\begin{aligned} &C_m^{(1)}(x,z,0) = C(x,0) && C_m^{(2)}(x,z,0) = C_0(x,z) - C_0(x,0) \\ &C_m^{(1)}(x,0,t) = C(x,t) && C_m^{(2)}(x,0,t) = 0 \\ &\frac{\partial C_m^{(1)}}{\partial z}(x,L_z,t) = 0 && \frac{\partial C_m^{(2)}}{\partial z}(x,L_z,t) = 0. \end{aligned} \tag{2.4}$$

The solutions for $C_m^{(1)}$ and $C_m^{(2)}$ can be expressed in the form [111]

$$\begin{aligned} C_m^{(1)}(x,z,t) =& C(x,t) - \frac{2}{L_z}\int_0^t \left(\sum_{n=0}^{\infty} \frac{1}{\lambda_n}\, e^{-D_a\,\lambda_n^2 (t-s)} \sin\lambda_n z\right) \frac{\partial C}{\partial s}(x,s)\, ds \\ C_m^{(2)}(x,z,t) =& \frac{2}{L_z}\sum_{n=0}^{\infty}\left(\int_0^{L_z} (C_0(x,y) - C_0(x,0)) \sin\lambda_n y\, dy\right) \\ & e^{-D_a\lambda_n^2\, t} \sin\lambda_n z, \end{aligned} \tag{2.5}$$

where

$$\lambda_n = \frac{(2n+1)\pi}{2L_z}. \tag{2.6}$$

Substitution of $C_m(x,z,t)$ to the first partial differential equation in Eq. (2.1) leads to an expression for C,

$$\begin{aligned} &\frac{\partial C}{\partial t}(x,t) + v\,\frac{\partial C}{\partial x}(x,t) = -\frac{2\epsilon\, D_a}{L_z\, b}\int_0^t \left(\sum_{n=0}^{\infty} e^{-D_a\,\lambda_n^2 (t-s)}\right) \frac{\partial C}{\partial s}(x,s)\, ds \\ &+ \frac{2\epsilon\, D_a}{L_z\, b}\int_0^{L_z} (C_0(x,y) - C_0(x,0)) \left(\sum_{n=0}^{\infty} \lambda_n\, e^{-D_a\lambda_n^2\, t} \sin\lambda_n y\right) dy. \end{aligned} \tag{2.7}$$

Introducing dimensionless variables

$$\xi = \frac{x}{L}, \quad \tau = \frac{t\,v}{L}, \quad \zeta = \frac{y}{L_z}, \tag{2.8}$$

Eq. (2.7) can be expressed in the form

$$\begin{aligned} &\frac{\partial C}{\partial \tau}(\xi,\tau) + \frac{\partial C}{\partial \xi}(\xi,\tau) = -\frac{2\lambda}{\kappa}\int_0^{\tau} \left(\sum_{n=0}^{\infty} e^{-(\gamma_n^2/\kappa^2)\,(\tau-\sigma)}\right) \frac{\partial C}{\partial \sigma}(\xi,\sigma)\, d\sigma \\ &+ \frac{2\lambda}{\kappa}\int_0^1 (F(\xi,\zeta) - F(\xi,0)) \left(\sum_{n=0}^{\infty} \gamma_n\, e^{-(\gamma_n/\kappa)^2\,\tau} \sin\gamma_n\zeta\right) d\zeta, \end{aligned} \tag{2.9}$$

and the initial and boundary conditions in the form

$$C(\xi,0)=F(\xi,0),\quad C(0,\tau)=f(\tau). \tag{2.10}$$

Here we have also used dimensionless parameters:

$$\lambda=\epsilon\,\frac{L}{b}\sqrt{\frac{D_a}{Lv}},\quad \kappa=\frac{L_z}{L}\sqrt{\frac{Lv}{D_a}},\quad \gamma_n=(n+\tfrac{1}{2})\pi, \tag{2.11}$$

and expressions

$$F(\xi,\zeta)=C_0(x,y),\quad f(\tau)=C_1(t) \tag{2.12}$$

for the initial and input concentrations of the tracer.

Laplace transformation of Eq. (2.9) with respect to variable τ gives

$$\begin{aligned}&\frac{\partial\hat{C}}{\partial\xi}(\xi,s)+(s+\lambda\sqrt{s}\tanh(\kappa\sqrt{s}))\hat{C}(\xi,s)=\\&\frac{2\lambda}{\kappa}\int_0^1 F(\xi,\zeta)\left(\sum_{n=0}^{\infty}\frac{\gamma_n\,\sin\gamma_n\zeta}{s+(\gamma_n/\kappa)^2}\right)d\zeta+F(\xi,0),\end{aligned} \tag{2.13}$$

and Laplace transformation of the boundary condition (Eq. (2.10)) gives

$$f(\tau)=\hat{f}(s). \tag{2.14}$$

The solution to Eq. (2.13) is given by

$$\begin{aligned}\hat{C}(\xi,s)=&\,\hat{f}(s)\,c(s,\xi)+\int_0^{\xi}c(s,\xi-\eta)\,F(\eta,0)\,d\eta\\&+\frac{2\lambda}{\kappa}\int_0^{\xi}\left\{\int_0^1 F(\eta,\zeta)\left(\sum_{n=0}^{\infty}\frac{\gamma_n\,c(s,\xi-\eta)}{s+(\gamma_n/\kappa)^2}\,\sin\gamma_n\zeta\right)d\zeta\right\}d\eta,\end{aligned} \tag{2.15}$$

where

$$c(s,\xi)=e^{-(s+\lambda\sqrt{s}\tanh(\kappa\sqrt{s}))\,\xi}. \tag{2.16}$$

The inverse Laplace transform of $c(s,\xi)$ is calculated explicitly in Appendix III, and it was found that

$$L^{-1}(c(s,\xi))=\Phi(\xi,\tau)=\begin{cases}\dfrac{4}{(\lambda\xi)^2}\,\Psi\left((\tau-\xi)/(\lambda\xi)^2,\kappa/\lambda\xi\right);\quad \tau>\xi,\\ 0;\quad 0\le\tau\le\xi.\end{cases} \tag{2.17}$$

Function Ψ can be given as a series expansion in terms of two functions,

$$f(x)=\frac{1}{\sqrt{\pi\,x^3}}\,e^{-\frac{1}{x}},\qquad g(x)=\frac{1}{\sqrt{\pi\,x}}\,e^{-\frac{1}{x}}, \tag{2.18}$$

in the form

$$\begin{aligned}\Psi(\alpha,\beta) = {} & f(4\alpha) + \frac{4}{z_1^3}\, g'\left(\frac{4\alpha}{z_1^2}\right) \\ & + \sum_{N=2}^{\infty} \frac{(-1)^N}{z_N^2} \left(\sum_{k=1}^{\left[\frac{N}{2}\right]} \frac{1}{(2k)!} \binom{N-1}{N-2k} \left(\frac{4}{z_N}\right)^{2k} f^{(k)}\left(\frac{4\alpha}{z_N^2}\right) \right. \\ & \left. - \sum_{k=1}^{\left[\frac{N+1}{2}\right]} \frac{1}{(2k-1)!} \binom{N-1}{N-2k+1} \left(\frac{4}{z_N}\right)^{2k-1} g^{(k)}\left(\frac{4\alpha}{z_N^2}\right) \right),\end{aligned} \tag{2.19}$$

where

$$z_N = 2N\beta + 1. \tag{2.20}$$

Using function Φ the solution to the problem Eq. (2.9) with the boundary and initial conditions of Eq. (2.10) can be expressed in the form

$$\begin{aligned}C(\xi,\tau) = {} & \int_0^{\tau} \Phi(\xi,\tau-\sigma)\, f(\sigma)\, d\sigma + \int_0^{\xi} \Phi(\xi-\eta,\tau)\, F(\eta,0)\, d\eta \\ & + \frac{2\lambda}{\kappa} \int_0^{\xi} \left\{ \int_0^1 F(\eta,\zeta) \right. \\ & \left. \times \left(\sum_{n=0}^{\infty} \gamma_n \int_0^{\tau} e^{-(\gamma_n/\kappa)^2(\tau-\sigma)} \Phi(\xi-\eta,\sigma)\, d\sigma\, \sin\gamma_n\zeta \right) d\zeta \right\} d\eta.\end{aligned} \tag{2.21}$$

In practical cases evaluation of the integrals in Eq. (2.21) may be done simply as Riemannian sums. After their numerical solution, transformation can be done back to physical variables and parameters. Notice that Eq. (2.21) allows the determination of tracer concentration anywhere in the porous matrix or in the flow channel. However, in order to compare the numerical results with the measured ones, only determination of $C(L,t)$ is needed. Notice also that the measured initial tracer concentration ($C_0(x,z)$) as well as the input tracer concentrations ($C_1(t)$) may be used as boundary and initial conditions (Eq. 2.2) when determining the breakthrough curve.

Function Φ is also a solution for a similar diffusion problem in the case of zero concentration initially in the flow channel and in the porous matrix, and for a delta-pulse input. Derivation of the solution is included in the enclosed Appendix III. In terms of physical parameters, the breakthrough curve can be expressed in the form

$$C_f(L,t) = \begin{cases} \dfrac{4M_0}{Q\,T}\, \Psi\left(\dfrac{t-t_0}{T}, \dfrac{L_z}{\sqrt{D_a\,T}}\right), & t > t_0, \\ 0, \quad 0 \le t \le t_0, \end{cases} \tag{2.22}$$

where

$$T = \frac{4\epsilon^2\, h^2\, L^2\, D_a}{Q^2}, \qquad t_0 = \frac{V}{Q}. \tag{2.23}$$

Here M_0 is the mass of the input tracer, $Q = 2\,h\,b\,v$ is the volumetric flow rate in the channel and $V = 2\,h\,b\,L$ is its volume. Notice that parameter t_0 does not affect the shape of the breakthrough curve, it only defines the time of breakthrough.

2.2 Experimental set-up for measuring breakthrough curves

In order to demonstrate different features of matrix diffusion and to validate the matrix diffusion modeling described above, an experimental system was constructed. The schematic layout of the system is shown in Fig. 2.2. This equipment consists of a water supply, peristaltic pump, injection system for the tracer, flow channel, porous matrix, precision scale, and PC-based control of the measurement system. Peristaltic pump was used to create water flow from the supply to the flow channel through an injection system. From the injection system the tracer, potassium chloride, was injected into the flow, and this system also stabilized the flow. A porous matrix made of synthetic dacron fibers lined to the flow channel is shown in Fig. 2.3. The porosity of compressed (h = 2.5 mm) dacron felt was measured by X-μCT, and was about 96 %. From the flow channel water was led to the precision scale which was used to measure the flow rate. In order to prevent evaporation, a thin layer of oil was placed on top of the collected water. Measurements were controlled, and the produced data were stored, by a PC-based control system.

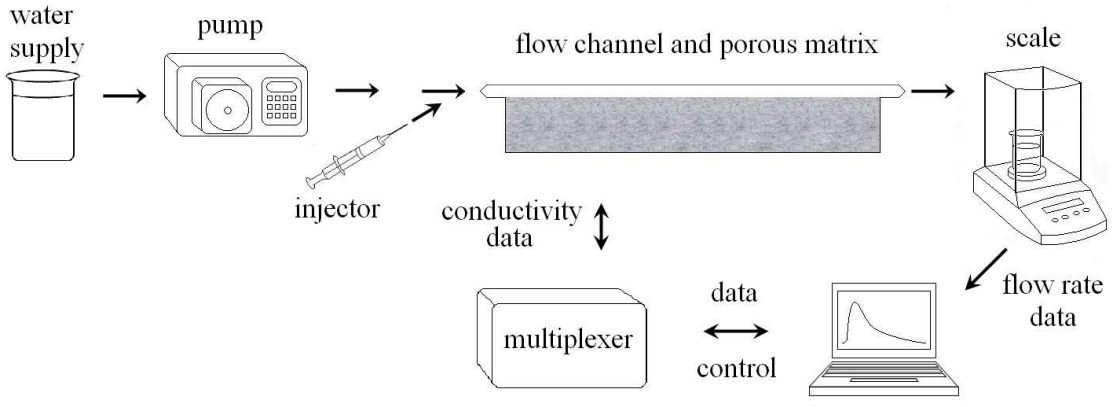

Figure 2.2. *Experimental equipment used for advection-matrix diffusion measurements. The system consists of water supply, peristaltic pump, tracer injector, flow channel, porous matrix, precision scale (to measure the flow rate), and a computerized operation and data collection system.*

Salinity of water strongly affects its conductivity, and tracer concentration can thus be measured by measuring the local conductivity of water. In order to measure the local conductivities, 128 electrode pairs were placed in the flow channel and in the porous matrix that lined one wall of the channel (see Fig. 2.3). In order to get information of the local conductivity, the voltages were measured over resistors of constant resistance placed in series with each pair of electrodes. Since conductivity is inversely proportional to resistance, voltage data contained information about the local conductivities. With this procedure voltage data were received, and later transformed into concentration data through a calibration curve. Conductivity measurements were done with a 50 Hz alternating current to prevent electrochemical processes [112].

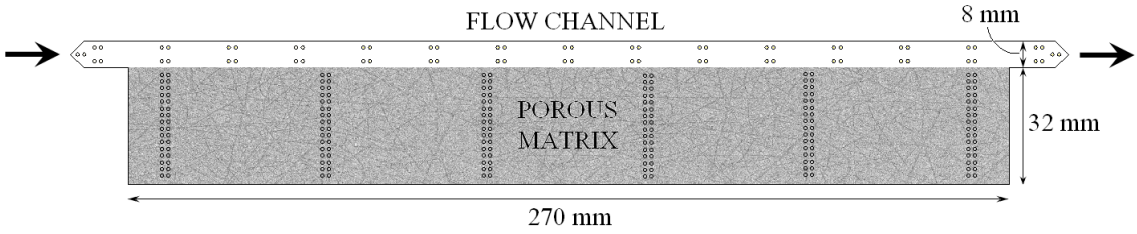

Figure 2.3. *Structure of the advection - matrix diffusion system showing the flow channel, porous matrix and arrangement of electrodes. The input electrodes were the first three pairs on the left before the beginning of the porous matrix, and the output electrodes, respectively, on the right. Thickness of the flow channel and matrix was* $h = 2.5$ *mm.*

Before measurements all electrode pairs were calibrated separately since they had unique voltage responses to varying salinity. Calibration was done by exposing all electrode pairs to an initially pure ion changed water (100 ml) whose salinity was then increased slowly by small controlled increments. Saline solution was mixed carefully so that a uniform salinity distribution was achieved before reading the voltages. The resulting calibration data for one input and output electrode pairs together with polynomial fits done to these data are shown in Fig. 2.4. Polynoms of rather high order had to be used as the second derivative of the curves typically had a negative sign at low salinities while it became positive for increasing salinity. Notice that in the output data only the low-salinity end of the calibration curve is usually needed. In Fig. 2.5a example curves of uncalibrated data are shown for electrodes located in the input, output, flow channel and porous matrix.

Flow rate fluctuated slightly during the measurements as shown in Fig. 2.5b. Changes for example in the temperature or resistance of flow may have caused such fluctuations. Also, the peristaltic pump affects the shape of the tube, which may cause drifting of the flow. Drift was typically higher for higher flow rates, but as will be seen below the effect of drift on the breakthrough curve (output) was negligible.

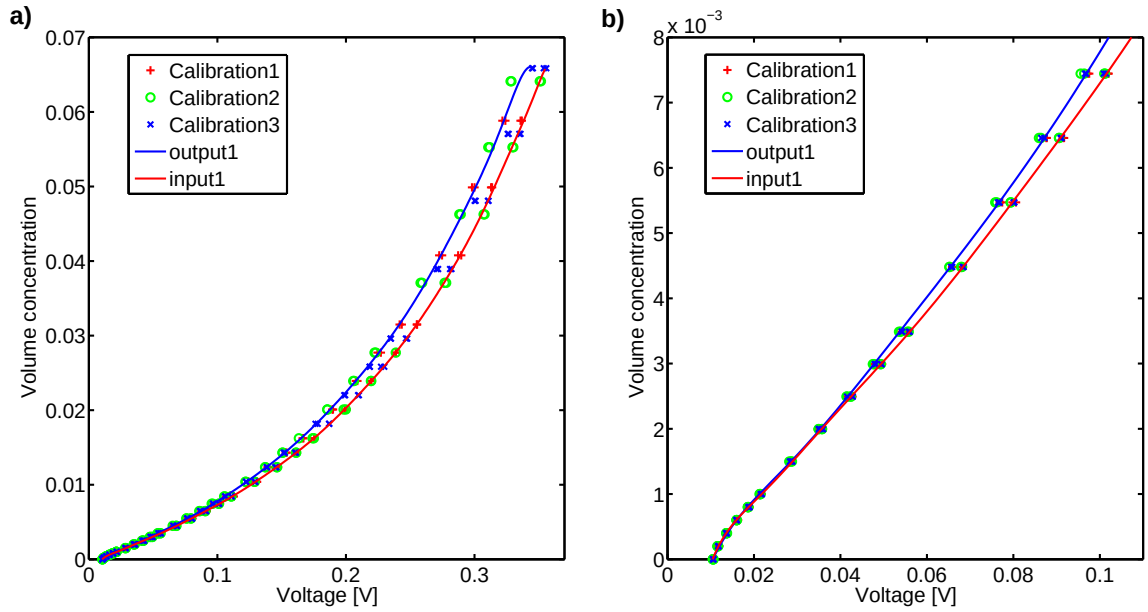

Figure 2.4. *Calibration curves for an input and output electrode showing the whole calibration range (a) and the typically needed calibration range (b). Note that volume concentration is used here.*

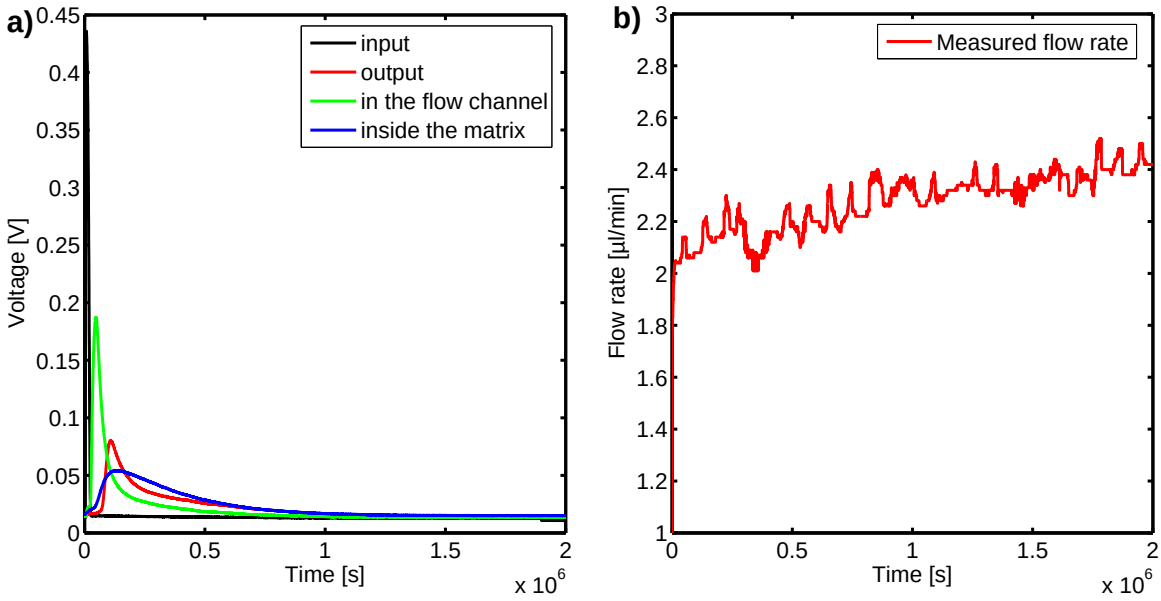

Figure 2.5. *a) Uncalibrated response to salinity pulse of conduction electrodes in the input (black), output (red), flow channel (green) and porous matrix (blue). b) Fluctuation of the flow rate (2 µl/min) during a typical measurement.*

2.3 Validation of the matrix diffusion model

For modeling the results of advection-matrix diffusion measurements, the solutions introduced in Sec. 2.1 were used. Two kinds of measurements were performed: 1. Measurements with a delta-function input and initially zero concentration in the porous matrix and in the flow channel. 2. Measurements with a delta-function input and an initially non-zero concentration in the porous matrix and in the flow channel. The first set of measurements was modeled by solving numerically Eq. (2.22), and the second set by solving Eq. (2.21), with appropriate boundary and initial conditions.

The first set of measurements was performed using various flow rates in order to see the effect of a matrix of a finite depth. In these measurements a 0.1 ml pulse of potassium chloride of given conductivity (this conductivity was taken to represent the maximum concentration in the analysis) was injected in fresh water flowing in the channel. In all measurements the input electrodes responded with a sharp peak to the injected pulse, which verified that the delta-function approximation could be used in the mathematical model, $C_1(t) = M_0\,(2h\,v\,b)^{-1}\delta(t)$. Flow rates of 1, 2, 4, and 8 μl/min were used, and otherwise the conditions were kept as constant. The measured breakthrough curves were then fitted by Eq. (2.22) using T and $L_z/\sqrt{D\,T}$ as the fitting parameters. The effects of longitudinal diffusion and Taylor dispersion were found to be vanishing in these measurements since parameter μ that indicated the magnitude of longitudinal diffusion and Taylor dispersion compared to advection in the flow channel, was found to be of the order of 10^{-2} (see Appendix III).

Experimental breakthrough curves fitted by the relevant model for the used flow rates are show in Fig. 2.6. The values $D_a = 2.0 \cdot 10^{-9}\mathrm{m}^2/\mathrm{s}$, $D_a = 1.9 \cdot 10^{-9}\mathrm{m}^2/\mathrm{s}$, $D_a = 2.1 \cdot 10^{-9}\mathrm{m}^2/\mathrm{s}$, and $D_a = 2.0 \cdot 10^{-9}\mathrm{m}^2/\mathrm{s}$ were obtained for the apparent diffusion coefficient in these four independent experiments. Excellent agreement between the measured and modeled breakthrough curves was found, which indicates that this model predicts all the relevant effects in the system in the used flow rate scale. In addition, the apparent diffusion coefficient determined is within the error bars the same as the result measured previously by completely different means [113], $D = 2.0 \cdot 10^{-9}\mathrm{m}^2/\mathrm{s}$. Note that in this case porosity is so high that it does not notably affect to diffusion coefficient.

For the fastest flow rate used (8 μl/min), the shape of the breakthrough curve was similar to the one for an infinite matrix (see Appendix III), which indicates that the effect of finite depth of the matrix was then negligible. When the flow rate was decreased, first a small hump appeared next to the primary peak (4 μl/min) and then the hump grew bigger (2 μl/min). When the flow rate was decreased even further, these two peaks were merged and formed one wider peak (1 μl/min). The observed

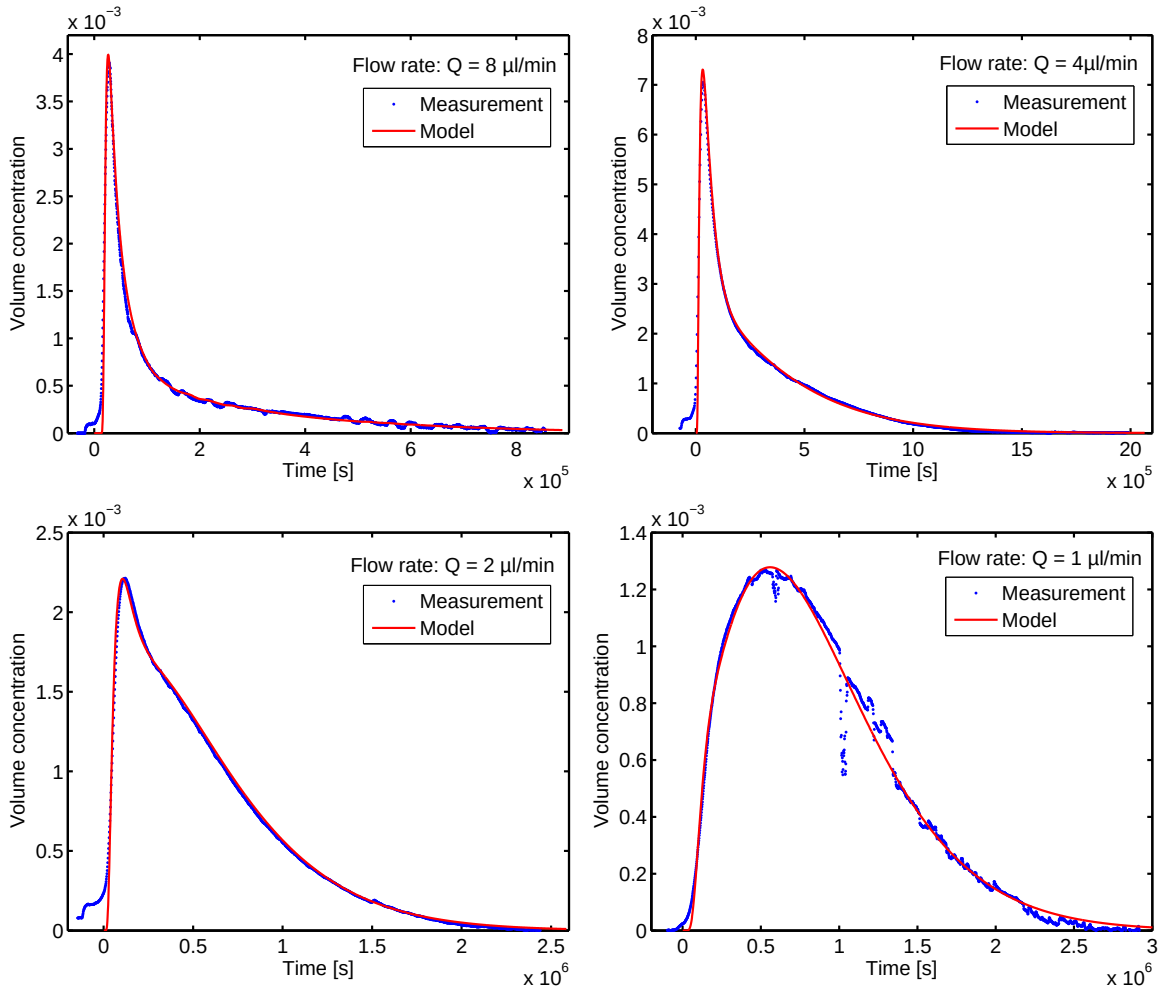

Figure 2.6. *Measured and fitted breakthrough curves for flow rates of 1, 2, 4, and 8 µl/min, used for validating the effects of a finite depth of the matrix. The measured breakthrough curves were fitted by Eq. (2.22).*

behaviour of the breakthrough curve is typical of diffusion in a matrix of finite depth. For fast flow rates the primary peak in the breakthrough curve was formed by tracer molecules that were migrating only by advection in the flow channel, and the tail of the peak was formed by the molecules that had diffused in the matrix and then returned back to the channel, but the average penetration depth of the molecules was not significant compared to the depth of the matrix. The appearing hump arises from tracer molecules that have reflected from the back wall of the porous matrix. When the flow rate is decreased further, the amount of molecules undergoing reflection becomes more significant compared to the ones migrating only by advection. In the case of an infinite matrix reflection does not occur, and such a hump does not appear.

In the case of an infinite matrix, the late time asymptotic tail that builds up in the breakthrough curve is a power law and decays as $t^{-3/2}$ [114]. For a matrix of finite depth, reflection of tracer molecules from the back wall changes the asymptotic behaviour, and such a pure power law is never formed. In the enclosed article of Appendix III it is shown that, in this case, the late time asymptotic behaviour of the breakthrough curve takes a rather different form,

$$C(L,t) \sim \frac{1}{t^{3/4}}\, e^{b\sqrt{t}-at}, \tag{2.24}$$

where a and b are constants depending on the parameters of the system.

The second set of two different measurements were performed using initially contaminated matrices, and non-zero initial concentrations $C_0(x,z) \neq 0$. As in the first measurement set, a sharp input pulse was used. However, when solving the problem mathematically, the actual measured input concentration, $C_1(t)$, was used instead of its delta function approximation. Also, the measured initial concentrations were used in the fitted function as $C_0(x,z)$. In the first measurement, a homogeneous initial potassium chloride concentration ($C_0(x,z) = C_0$) was used. As in the first measurement set, a 0.1 ml pulse of potassium chloride was then injected into the flow, after which flow of fresh water was introduced in to the system (see Fig. 2.7, input curve on the left panel). In the second measurement, an inhomogeneous initial potassium chloride concentration profile ($C_0(x,z)$) was added, otherwise the measurement was similar. In both measurements the flow rate was set to 4 μl/min in order to have some influence of the finite depth of the matrix on the breakthrough curve, observed in the first set of measurements (see Fig. 2.6).

Measured input and breakthrough curves together with fits by Eq. (2.21) are shown in Fig. 2.7. In both measurements the input curves (the upper panels in Fig. 2.7) show a sharp pulse of tracer followed by a rapid drop of concentration due to incoming fresh water. Here a small background concentration of potassium chloride was used in order to have a clear difference between the two contributions (see below). The dimensionless parameters λ and κ (Eq. (2.11)) were used as the fitting parameters

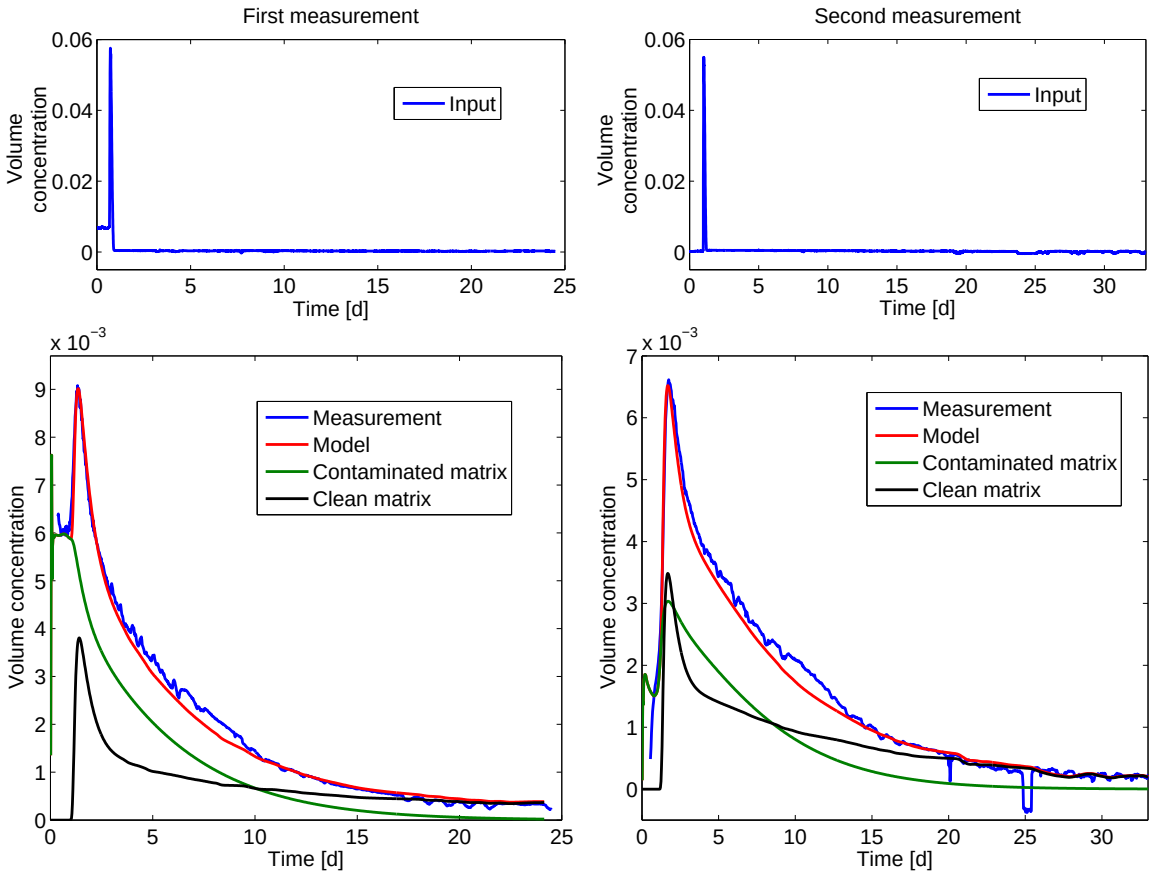

Figure 2.7. *Measured and fitted breakthrough curves (lower panels) together with input curves (upper panels) in the case of initially contaminated matrices. In two different measurements a constant (left panels) and varying (right panels) initial concentration inside the matrix was used. Fittings were done by the related theoretical expressions (Eq. (2.21), and were divided into two contributions, one from the contaminated matrix and another from the input concentration.*

when determining the theoretical breakthrough curves. From the fitted values of λ and κ, the values $D_a = 1.8 \cdot 10^{-9} m^2/s$ and $D_a = 1.9 \cdot 10^{-9} m^2/s$ for the apparent diffusion coefficient were determined. Again, the determined values of the diffusion coefficient are similar to previously measured ones [113].

Excellent agreement between the measured and modeled breakthrough curves indicates that the model used predicts all the relevant migration processes occurring in the measurement system. The resulting breakthrough curves can also be divided into two components that arise from: 1. The tracer coming along the flow (black curve in Fig. 2.7), and 2. The tracer existing initially in the porous matrix and in the flow channel (green curve in Fig. 2.7). In Eq. (2.21) the first term corresponds to the input concentration and the second and third terms to the contaminated matrix. Once again, the humps appeared next to the primary peaks (black curves in Fig. 2.7) indicating effects arising from the finite depth of the matrix. As for tracer initially in the matrix, the obvious slow decay of concentration can be observed (green curves in Fig. 2.7).

Chapter 3

Structure characterization of geological materials

In this chapter, special attention is paid to introducing a method which combines results of structure, pore space and mineral composition as obtained by using X-ray micro computed tomography (X-μCT) and the ^{14}C-labeled-polymethylmethacrylate (^{14}C-PMMA) method. As a result we get a 3D porosity map together with information of porosity distribution, pore size distribution and mineral abundances. The characterization procedure is presented here by using altered Sievi tonalite as an example. However, the procedure introduced here can also be implemented for various porous materials. In the enclosed articles in Appendices I and IV, a closer overview is given to altered Sievi tonalite, its minerals, and sample characteristics.

3.1 X-μCT imaging and image analysis

In general, X-ray tomography is used to obtain a 3D digital representation of a sample under examination. The method is based on detecting differences in the X-ray attenuation inside the sample using 2D X-ray projection images. These projection images, taken from different directions are then converted to a 3D representation of the sample using computational reconstruction. Typically the projection images are obtained by exposing the sample to X-rays while stepwise rotating it with small (constant) increments around its axis. A few hundred to 2000 projection images are usually taken for reconstruction, using either a 180 or 360 degree rotation. [115, 116, 117]

In other words X-ray tomography produces a 3D matrix of local X-ray attenuation co-

efficients. Generally the attenuation coefficient is proportional to the material density and elemental composition of the sample [118, 119, 53]. Hence the above data matrix may be considered as a 3D density map of the sample. In geological materials various properties, e.g., purity of minerals and their state of alteration influences their density and further the X-ray attenuation [120, 53]. However, occasionally it is possible to bind minerals with similar attenuation into one mineral group as e.g. in the enclosed article of Appendix IV.

In this work reconstructions of rock samples for their structural analysis were obtained using a table-top X-μCT scanner (SkyScan 1172) based on a conventional X-ray tube with a spot size less than 5 μm (see Fig. 3.1). First the scanner converts X-rays coming through the sample to visible light by applying a scintillator plate and then detects them with a 2D CCD chip. The projection images were filtered by averaging over 10 images taken in the same position. The inversion problem in the reconstruction was solved using the Feldkamp algorithm which is often applied when a conical-beam table-top scanner is used [121]. Conical beam has the advantage of continuously varying the voxel resolution with varying sample size. The voxel size of the scanner can be varied from 0.9 to 30 μm, while the maximum diameter of the sample varies from 2 to 68 mm, respectively.

Figure 3.1. *A table-top X-μCT scanner, SkyScan 1172, used in this work.*

Here X-μCT images were taken with various voxel sizes: 3.5, 6.9, 14.4, and 21.1 μm. Voxel sizes from 6.9 μm to 21.1 μm were used to scan samples (B_1, B_2, and B_3) with a maximum horizontal dimension of 25 mm (see Fig. 3.2a), and a voxel size of 3.5 μm for 9 mm sized subsamples (B_{21} and B_{22}). The aim in using different scanning resolutions was to study the influence of scanning resolution on the detected abundances of different components and determined pore connectivity. In 3D reconstruction of sample B_1, shown in Fig. 3.2b, pores appear as dark areas, feldspar and its alteration products as dark gray, mica and its alteration products as light gray, and dense accessory or secondary minerals, such as hematite, goethite, zircon, titanite, apatite and monazite, as small-sized white spots. The minerals in each group were first identified using scanning electron microscope (SEM) and energy dispersive X-ray analyses and

then linked to tomographic reconstructions. In order to conserve simplicity altered feldspar refers to feldspar and its alteration products, and altered mica to mica and its alteration products, respectively, from here on.

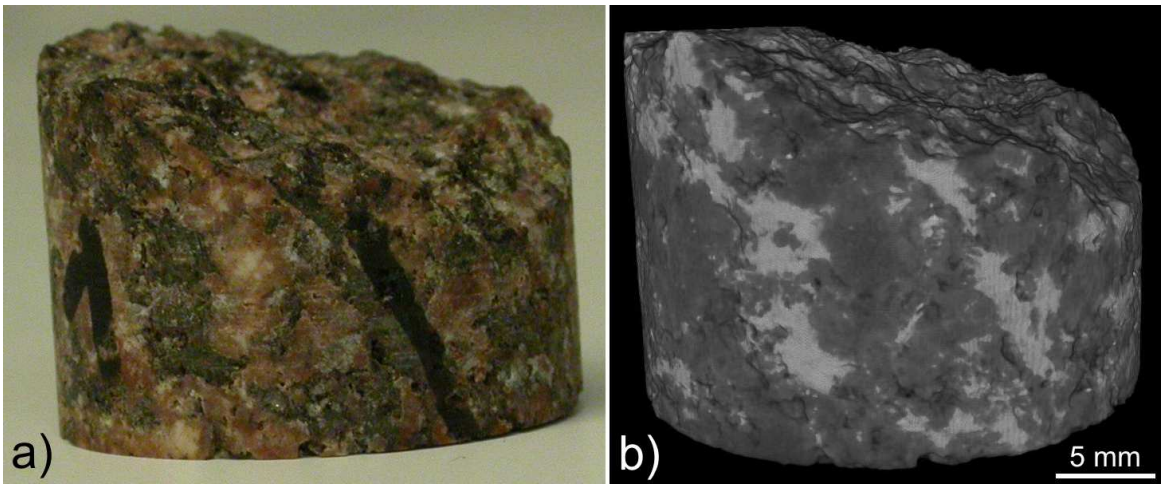

Figure 3.2. *Sample B_1 of altered Sievi tonalite (a) together with a corresponding 3D tomographic reconstruction (b). Lighter shade of gray corresponds to higher attenuation of X-rays and, typically, higher density.*

Typically analysis of tomographic images requires various tools to enhance the image quality and detectability of details, as well as segmentation tools. Here, before quantitative structural analysis, noise in the original 3D gray scale images (see Fig. 3.3a) were reduced by applying a nonlinear variance-based filter [122]. The air surrounding the sample was segmented with a surface detection algorithm based on a discrete and quenched version of the Edwards-Wilkinson equation [123]. For segmentation of different components in the samples, a method was used based on finding the thresholding values by fitting normal and log-normal distributions to each peak in the grayscale histogram, and selecting the best possible combination. In Figure 3.3b an example is shown of the resulting images, which contains different mineral groups listed above. After the image treatment, connectivity of pores was determined from the tomographic reconstructions using a region-growth algorithm [122]. Pore size distributions of the tomographic reconstructions were determined using the watershed algorithm [124, 122, 125, 126, 59]. More detailed descriptions of these tools and algorithms are found in the references of Appendix IV.

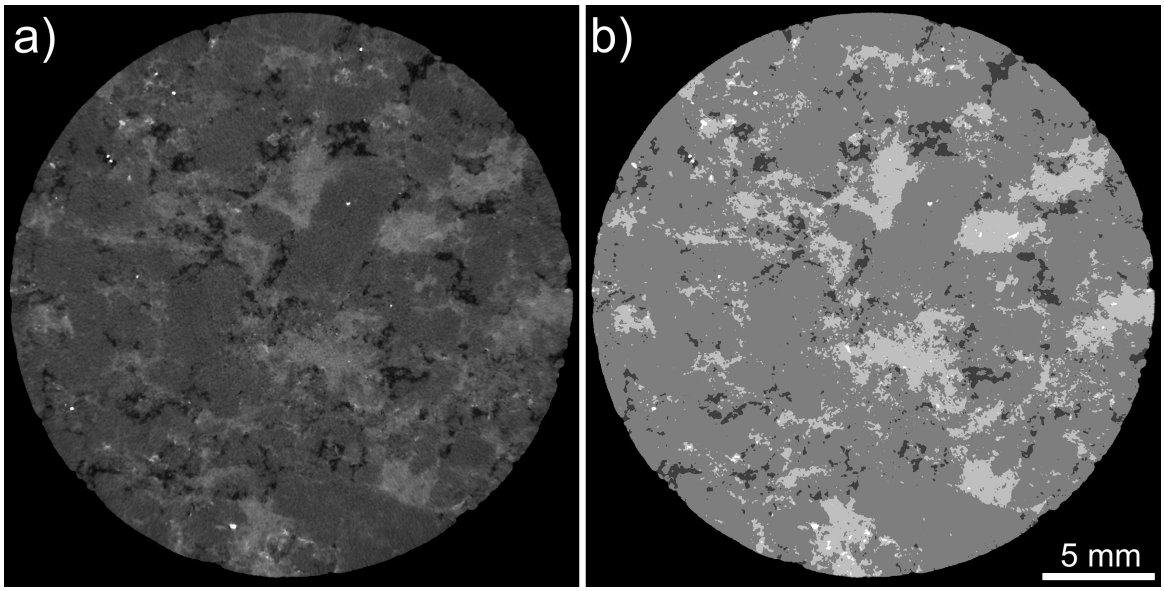

Figure 3.3. *Shadowgram images by a X-μCT-scanner are first reconstructed to 2D cross section images (a), after which noise may be filtered from the images and different components segmented (b). In the images lighter shade of gray corresponds to higher attenuation of X-rays and, usually, higher density.*

3.2 Implementation of ^{14}C-PMMA method

The ^{14}C-PMMA method can be used to study the porosity and pore structure of rock samples in centimeter scale. The method provides a 2D porosity distribution of the connected pores. Together with a petrographic mineral characterization, these images provide information of the intra- and intergranular porosity. [75, 78]

The ^{14}C-PMMA method involves impregnation of the rock sample with ^{14}C-labeled MMA in vacuum, polymerization of MMA by irradiation or heating, film or digital autoradiography, determination of optical densities by digital image processing techniques, and determination of porosities by image analysis. The low molecular weight and low viscosity of the carrier monomer MMA provides direct information about the accessible pore space in the rock. Applied to rocks of low porosity, autoradiography provides the spatial distribution of the porosity, in contrast to commonly used bulk porosity measuring methods.

Before impregnation by MMA, sample is dried to remove water from pore space, which could prevent the intrusion of the monomer. Drying of the sample is done in vacuum using a temperature of 50 °C to 120 °C, for a few days to a month depending on the

sample. During drying, the weight loss (i.e. evaporated water) of the sample may also be monitored. When the weight of the sample does not change significantly any more, most water has been evaporated from the pore space and it is ready for impregnation.

Impregnation of ^{14}C-MMA is performed in the same vacuum chamber as drying. First the chamber is filled with ^{14}C-labeled MMA gas and then it is filled with ^{14}C-labeled MMA liquid. The monomer intrudes first large pores due to capillary forces, and subsequently also small pores. The time needed for impregnation highly depends on the total porosity, sample size, connectivity, and structure of pore space (tortuosity and constrictivity). Typically impregnation times vary from a few days to a month.

MMA is polymerized (to PMMA) using radiation by a ^{60}Co source. Typically, a total dose of 50-80 kGy is suitable for centimeter scale rock samples [78]. Polymerization could also be done using heat or chemical initiation [127, 128, 129].

Film or digital autoradiography is used to detect the amount of β-particles emitted by the ^{14}C-PMMA in the sample. A polished sample surface is placed next to an autoradiographic X-ray film which contains silver halogenide crystals for detection of the β-particles. Radiation reduces silver ions to metallic silver on the film. When the autoradiographic films are developed, the region of the rock which contains more ^{14}C-PMMA reduces more silver halogenide grains, and the corresponding area on the film appears darker than the areas with less radiation (see Fig. 3.4b). Since the ^{14}C-particles are located only in the pore space, the blackening of the film is proportional to porosity. For typical available autoradiographic films, the best possible resolution of the ^{14}C-PMMA method is about 20 μm. [78]

Autoradiographs are converted to digital format using a CCD camera or a table scanner, both of which provide gray scale images. The resolution used in this conversion defines the final size of the pixel and thus the final resolution of the autoradiographic image. In the case of ^{14}C, a better resolution than 1200 dots per inch (dpi, 21.2 μ) is not beneficial due to the resolution of the method. Typically a resolution of 600 dpi (42.5 μ) is used.

In the following the mathematical and physical background of the ^{14}C-PMMA method is explained following the references [75, 78]. In principle, from blackening of the film caused by radiation emitted by the rock surface, the amount of tracer in the sample can be determined, and it is proportional to porosity. If the pore sizes are well below the resolution of the autoradiography (42.5 μm in the present case), a major fraction of the emitted β-radiation is attenuated by the rock matrix, and the determination of porosity is more reliable. In such a case the tracer can be considered to be virtually diluted by the rock matrix. The error is also small when the sizes of fissures are below a micrometer scale (dimensions of pores and fissures are small relative to the

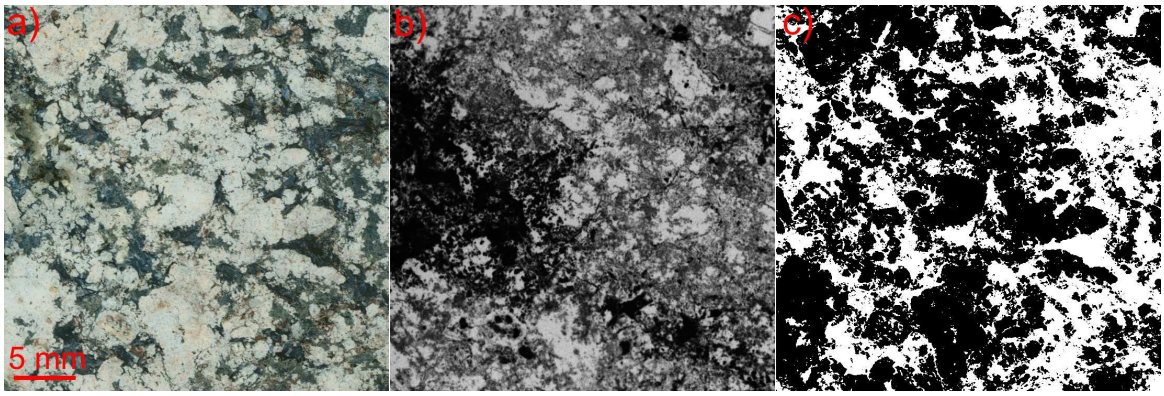

Figure 3.4. *a) Stained rock surface showing altered mica (dark areas) and altered feldspar (light areas). b) A ^{14}C-PMMA autoradiograph of the same rock surface in which light shades of gray correspond to low porosity and dark shades to high porosity. c) A segmented binary image of the same rock surface showing areas of altered mica (white) and altered feldspar (black).*

range of β-absorption). However, when zones of fissures and cracks of a micrometer or millimeter scale are present in rock, the dilution assumption is not valid. These fissures and cracks increase the uncertainty of the porosity determination, and thus it is better to exclude these areas from the quantitative porosity determination. On the other hand, the porosities determined by the ^{14}C-PMMA method for clays are valid using since in clays most of the pores are in a nanometers scale [130].

The gray values of the digitized autoradiographs may be considered as intensities (I) and may therefore be converted to optical densities (OD) according to the Beer-Lambert law:

$$OD = -log(\frac{I}{I_0}), \tag{3.1}$$

where I_0 is the background intensity. Furthermore, a calibration function is needed from activities to optical densities. Calibration is done by measuring the optical densities of ^{14}C-PMMA standards with known activities (A), and fitting an exponential calibration function

$$OD = OD_{max} - OD_0 e^{-kA}, \tag{3.2}$$

where OD_{max}, OD_0, and k are fitting parameters to the measured optical densities. Solving for the activity it is found that

$$A = -\frac{1}{k} \ln \left(\frac{OD_{max} - OD}{OD_0} \right), \tag{3.3}$$

which can be used for converting the intensities of individual pixels in an autoradiograph to activities.

β-particles emitted by ^{14}C may be absorbed by the material they are traversing, and the absorption rate depends on the material. A β-correction factor is needed since the absorption rate in rock differs from the absorption rate in PMMA. In this case the material consists of rock and the pore space is filled by PMMA. A rough approximation is that absorption of radiation depends linearly on density, and thus the β-correction factor can be considered to be a ratio of the density of the sample (ρ_s) to that of pure PMMA (ρ_0). On the other hand, in a two component system, the sample density depends on porosity (ϵ), density of rock (ρ_r) and density of pure PMMA. On these bases (density corrected) β-correction factor can be expressed in the form

$$\beta = \frac{\rho_s}{\rho_0} = \frac{\epsilon\rho_0 + (1-\epsilon)\rho_r}{\rho_0}. \tag{3.4}$$

Next the activities can be converted to porosities. It can be assumed that ^{14}C-PMMA is diluted by porous rock and the majority of β-radiation is absorbed by the rock. The local porosity can be considered to be a ratio of the β-corrected local activity (A) and to that of pure ^{14}C-PMMA (A_0), so that

$$\epsilon = \beta\frac{A}{A_0} = \frac{\rho_r/\rho_0}{1 + (\rho_r/\rho_0 - 1)A/A_0}\frac{A}{A_0}, \tag{3.5}$$

Notice that equations (3.1)-(3.5) are used for determination of local variables in each pixel of the autoradiograph. When determining the total porosity or the porosity of a specific area, an average of local porosities is used, and the former quantity e.g. is given by

$$\epsilon_{tot} = \frac{\sum_{n=0}^{N} A_n\epsilon_n}{\sum_{n=0}^{N} A_n} = \frac{\sum_{n=0}^{N} \epsilon_n}{N}, \tag{3.6}$$

where N is the number of pixels, A_n the area of pixel n and ϵ_n the porosity of pixel n.

In this work samples were dried at 100 °C in vacuum for one week, followed by impregnation by ^{14}C-labeled MMA (activity 925 kBq/ml). Then MMA was polymerized with a ^{60}Co-source (total dose 68 kGy). After irradiation the sample was sawed into pieces, and the studied surfaces were polished and autoradiographs were taken by exposing Kodak MR autoradiographic films with them. The exposure time varied from 5 to 7 days. The 2D autoradiography films were then digitized to 8-bit gray value images using a table-top scanner (CanoScan 9900F, maximum optical resolution 2400 dpi) with a resolution of 600 dpi (pixel size 42.5 μm). The gray scale values of the autoradiographs were then converted first to optical densities and then to porosities using Eqs. (3.1)-(3.5) and the procedure described above.

For the porosity determination of an individual mineral phase one has to examine an area of the autoradiograph which corresponds to that mineral. To this end, chemical

staining of minerals may be used to assist the segmentation of different minerals at the rock surface [131, 73]. Staining chemicals depend on the mineral composition [132], and typically a precise mineral identification is needed before staining. A stained surface can be segmented into different mineral phases using, e.g., the k-mean cluster algorithm [133, 134, 135, 136]. This algorithm is based on three steps:

1. Selection of means of clusters (seed pixels).
2. Assignment to a cluster of each point based on the shortest distance to the mean of the cluster.
3. Determination of new means as the average position of the points in each cluster.

The last two steps are repeated until the means of the clusters do not change any more or no point changes its cluster. Various procedures have been developed to handle problems related to selection of the location and number of the seed pixels [137, 138, 139]. The segmented image has to be superimposed with the corresponding autoradiograph in order to have information about the intragranular porosity. The intragranular porosity of each mineral phase can be determined using Eq. (3.6).

In Fig. 3.4a a stained rock surface is shown. In this case the surface was first held in HCl solution for a minute to clean its surface. Then it was etched in a 40% HF solution for another minute to whiten the altered feldspar. Finally, the sample surface was put in contact with K-ferrocyanide, in order to make the altered mica blue. After this the surface was optically scanned in 24-bit RGB (red-green-blue) format using 600 dpi resolution, and then segmented using the k-mean cluster algorithm (see Fig. 3.4c). In the present case a usual problem related to the selection of seed pixels was avoided since the amount of components (k=2) was known and thus could be selected manually at the surface. Distances from the cluster centers were determined as Euclidian distances in the RGB space, and the algorithm was iterated until no pixel changed its cluster. Here the areas which were fully saturated in the autoradiograph ($\epsilon = 100\%$) were excluded from the analysis of intragranular porosities.

3.3 Results and outcome of combination of analysis methods

After noise reduction, surface detection and component segmentation, using the methods introduced in Appendix IV, the detected porosity, abundances of different minerals

Table 3.1. *Porosities, abundances of different minerals, and pore connectivities of altered Sievi tonalite determined from tomographic reconstructions for varying voxel size.*

Voxel size (μm)	Porosity [%]	Altered felspar [%]	Altered mica [%]	Accessories [%]	Pore connectivity [%]
3.5	6.3 ± 0.4	71 ± 2	22 ± 1	0.9 ± 0.1	-
6.9	5.8 ± 0.4	72 ± 2	22 ± 2	0.10 ± 0.02	81 ± 6
14.4	5.0 ± 0.4	73 ± 2	22 ± 2	0.20 ± 0.03	52 ± 5
21.1	4.5 ± 0.4	78 ± 2	17 ± 2	0.10 ± 0.02	50 ± 5

and connectivities of detected pores were determined from the tomographic reconstructions for each voxel size (see Table 3.1). It was evident that the number of pores and the content of accessory minerals increased with decreasing voxel size indicating that a detectable amount of pores and grains of accessory minerals had a size close to the voxel sizes used. As for altered feldspar and altered mica, their abundances did not change significantly for voxel sizes smaller than 14.4 μm indicating that their typical grain size was larger than the resolution. In addition, these observations were verified by SEM analysis as well as visual comparison of tomographic reconstructions.

The pore connectivities shown in Table 3.1 were defined by the part of the pores that were connected through the pore space to sample surface. As presumed, connectivity increases with decreasing voxel size. Connectivity has a faster rise somewhere in between voxel sizes of 14.4 and 6.9 μm indicating that an important amount of pore throats had a size close to these voxel sizes. Connectivity was not determined for a voxel size of 3.5 μm since, due to the smaller sample size of these subsamples, the results would not have been comparable to the ones determined for larger samples, but it was expected to increase further with decreasing voxel size. Generally, a significant amount of the pores detected by X-μCT was connected, which was likely caused by alteration since this kind of pore network rarely exists in fresh rock.

Evidently pores smaller than the used voxel size could not be detected by X-μCT, and thus the resulting porosity values obviously underestimated the true porosity. To this end the total porosity was also measured using argon pycnometry (see Appendix IV), and a total porosity of 10.6% was determined. Hence, from 41 to 58% of the pores remained undetected by X-μCT depending on the voxel size. These pores were expected to be located inside the mineral grains as intragranular porosity. The ^{14}C-PMMA method did not have a similar restriction and thus it was used to analyze the intragranular porosity (for results, see below).

In order to have a conception of how porosity of the rock as detected by X-μCT varies over small volumes, the porosities of 4×4×0.4 mm^3 -sized volumes of samples B_{21} and B_{22} (voxel size 3.5 μm) were determined. The chosen control volume exceeds the typical grain size of the minerals, and thus its size was found sufficient. Porosities of these control volumes ranged from 0 to 20%, and the resulting porosity distribution had a maximum at 4-5% (see Fig. 3.5). The determined porosity distribution was also fitted by a log-normal distribution and rather nice correspondence was found between the fitted and measured distributions. Log-normal distributions of similar quantities are found quite often in nature [140].

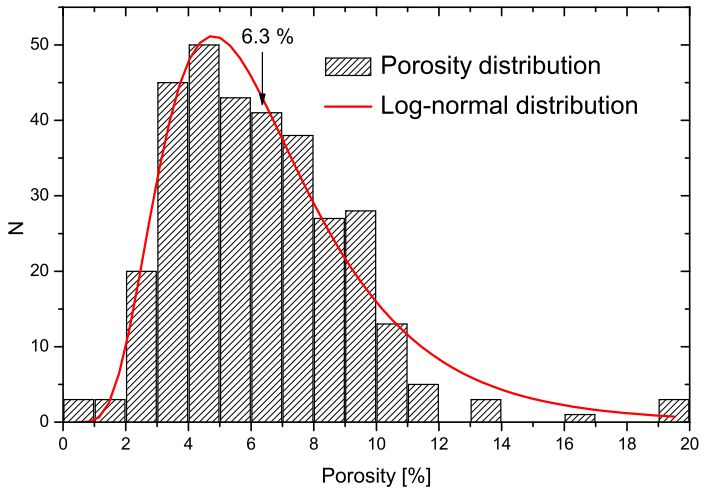

Figure 3.5. *Distribution of the porosities of 4x4x0.4 mm^3 volumes of a tomographic reconstruction with a 3.5 μm voxel resolution of two samples of Sievi tonalite. Using this resolution, the porosity of the entire sample was 6.3%. A fit by a log-normal distribution is also shown.*

The pore spaces segmented from tomographic reconstructions may be used to determine a pore size distribution. To this end, first the pores were segmented using the watershed algorithm and then their diameters were determined using equivalent spheres. This treatment was done for samples B_{21} and B_{22} which were scanned with a resolution of 3.5 μm. In the resulting pore size distribution shown in Fig. 3.6, each column shows the amount of pores with a diameter in a 3.5-μm-wide interval. The analysis revealed that pore sizes from 3.5 μm to 700 μm were found from these samples. However, pores having a larger diameter than 100 μm were excluded from the graph due to their poor statistics. Here a log-normal distribution fitted to the whole distribution did not lead to a best possible agreement. However, a sum of separate fits to small and large pore sizes gave an excellent agreement with the data over the whole

size range (see Fig. 3.6). This kind of behaviour indicates that small and large pores may be created by different processes. Similar analyses done of other reconstructions for larger voxel sizes (6.9, 14.4, and 21.1 μm) lead to similar results. Pore sizes of up to 1.1 mm were found.

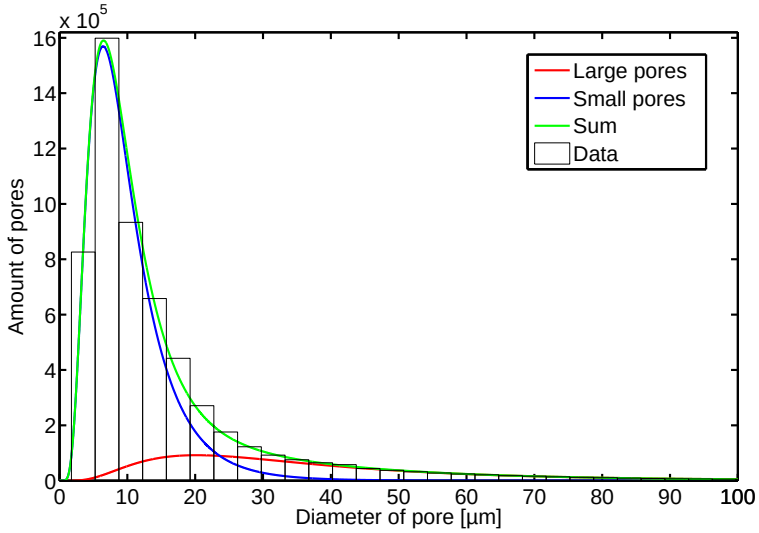

Figure 3.6. *Pore size distribution of a sample scanned with a 3.5 μm voxel size. A log-normal distribution was fitted to small (blue) and large (red) pore sizes of the distribution. The sum of the fitted distributions is also shown (green). The bar width used in the distribution was 3.5 μm.*

The ^{14}C-PMMA method was applied for 20 altered Sievi tonalite surfaces (see Fig. 3.4b) in order to get information about the pore space and intragranular porosities that had remained undetected by X-μCT. Analysis of autoradiographs shows that altered feldspar and altered mica are both porous, which was also confirmed by SEM analysis. Analysis of autoradiographs gave 9.3% for the average porosity of 20 surfaces, while the porosities of individual pixels varied from 0% to 100% with a median between 2% and 3%. The value determined for the total connected porosity is in good agreement with the result of argon pycnometry (ϵ = 10.6%), especially when considering the limitations of the ^{14}C-PMMA method. Intragranular porosities of altered feldspar and altered mica were determined by staining the minerals and segmenting them using the k-mean cluster algorithm. The resulting average porosities of altered feldspar and altered mica were 4.5% and 8.6%, respectively.

The intragranular porosities were determined above by the ^{14}C-PMMA method for altered feldspar and altered mica, while the 3D distributions of these minerals were determined by X-μCT. These two results were combined such that the average porosity of each mineral was assigned to that mineral phase in the tomographic reconstruction. Large pores, detectable by X-μCT, were treated separately, and appear as such in the

porosity distribution. Using such a procedure, 3D porosity maps for samples of Sievi tonalite were constructed. An example of a 3D porosity map is shown in Fig. 3.7.

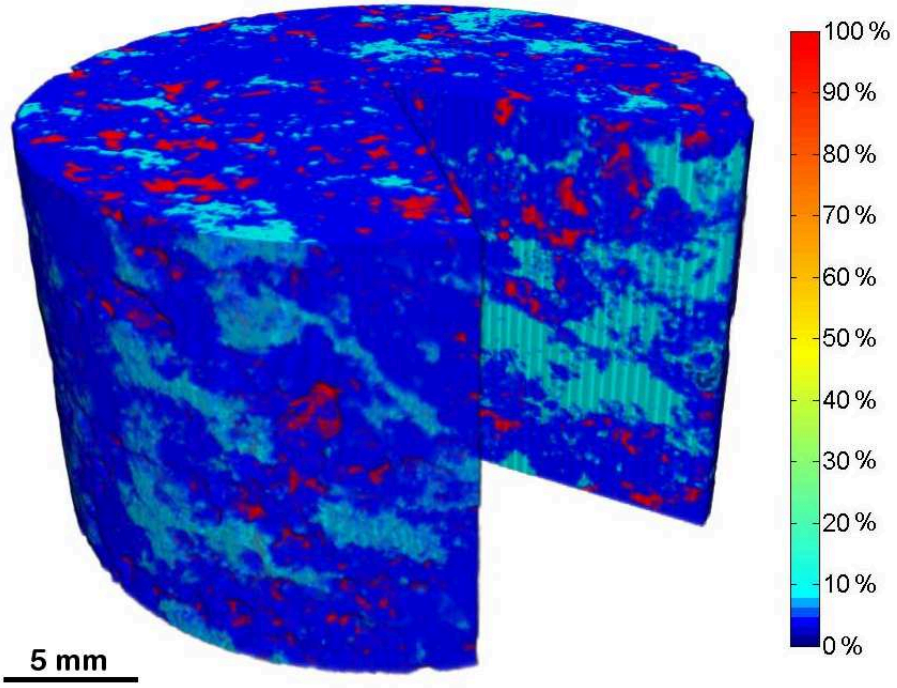

Figure 3.7. *Three dimensional porosity map of a sample of Sievi tonalite. Altered feldspar appears blue (porosity 4.5%), altered mica light blue (8.6%), large pores red (100%), and accessory minerals are dark blue (0%). The diameter of the sample is 25.1 mm, and the voxel size is 21.1 μm.*

Chapter 4

3D diffusion with time domain simulations

In this chapter rock structure characterization and diffusion processes are combined by simulating diffusion in 3D samples. Simulations are carried out by the time domain diffusion (TDD) method which is a rapid particle tracking method. The objective was to validate the TDD method in 3D, and to show that this method can be used to simulate diffusion in heterogeneous porous rock. Here Sievi tonalite was used as a test case, for which the 3D porosity map was constructed earlier (see Fig. 3.7).

4.1 The time domain diffusion model

The time domain diffusion (TDD) method was used to simulate diffusion in various cases ranging from validation of the method to studying the effect of heterogeneous distribution of porosity in Sievi tonalite. The TDD method was originally developed to simulate diffusion in 2D porosity maps generated by the ^{14}C-PMMA method [101, 104]. It is especially convenient when dealing with large systems since computation times do not considerably depend on sample size, and it is faster than more traditional simulation methods [104]. In the TDD method a particle is forced to jump at each simulation step to one of its neighbouring voxels. As for traditional methods, a particle may do numerous tries before a successful jump.

As mentioned earlier, construction of the method was inspired by and modified from a continuous time random walk method developed to study the permeability and conductivity of heterogeneous materials [103]. The physical background behind the

TDD method is explained and the relevant equations are derived here following the references [101, 102, 104]. In a heterogeneous porous medium, the diffusion equation can be written in the form

$$\frac{\partial(\epsilon C)}{\partial t} = \nabla \cdot (\epsilon\, D_a \cdot \nabla C), \tag{4.1}$$

where ϵ is the porosity of the medium, C the volumetric concentration of the diffusing tracer and D_a apparent diffusion coefficient. Using the divergence theorem and a finite volume formalism, this equation can be expressed in the form

$$\epsilon_i V_i \frac{\partial C_i}{\partial t} = \sum_j A_{ij} (\epsilon D_a)_{ij} \frac{C_j - C_i}{L_{ij}}, \tag{4.2}$$

where subscript i refers to a particle's initial position, subscript j refers to all the possible positions next to position i (see Fig. 4.1), V_i is the volume of position i, C_α the mean concentration of tracer at position α ($\alpha = \mathrm{i}, \mathrm{j}$), L_{ij} the distance between the centers of positions i and j, A_{ij} the area of the interface between these positions, $(\epsilon D_a)_{ij}$ the harmonic mean of the product of porosity (ϵ) and apparent diffusion coefficient (D_a) at positions i and j. The harmonic mean is required in order to conserve the mass balance between the positions. Denoting

$$b_{ij} = \frac{A_{ij} (\epsilon D_a)_{ij}}{L_{ij}}, \tag{4.3}$$

and since in the Lagrangian framework partial derivative respect to time is equivalent to material derivative, Eq. 4.2 may be written in the form

$$\epsilon_i V_i \frac{dC_i}{dt} = -C_i \sum_j b_{ij} + \sum_j b_{ij} C_j. \tag{4.4}$$

And further, by reordering terms, it can be expressed in the form

$$\frac{\epsilon_i V_i}{\sum_j b_{ij}} d(\log C_i) = -dt + \frac{\sum_j b_{ij} C_j / C_i}{\sum_j b_{ij}} dt. \tag{4.5}$$

Dimensional analysis of Eq. (4.2) shows that dimension of b_{ij} is $[L^3 T^{-1}]$, which is proportional to volumetric flux by diffusion between positions i and j, and, therefore,

$$P_{ij} = \frac{b_{ij}}{\sum_j b_{ij}}, \tag{4.6}$$

is nothing but the transition probability from position i to position j. Note that for an impermeable voxel ($\epsilon = 0$ of $D_j = 0$) b_{ij} becomes to zero, which leads to vanishing transition probability. Furthermore, for single particle initially at point i, last term in Eq. (4.5) vanishes [106], and we find that

$$dt = -\frac{\epsilon_i V_i}{\sum_j b_{ij}} d(\log C_i). \tag{4.7}$$

Hence, a particle at position i will jump to position j with a transition probability P_{ij}, and the time of diffusive transition from i to j is given by [106]

$$t_{i\to j} = -\frac{\epsilon_i V_i}{\sum_j b_{ij}} log(u_{01}), \tag{4.8}$$

where u_{01} is a random number from a uniform distribution between 0 and 1.

In an actual simulation, an initial position for each particle was first chosen randomly in the reservoir (depending on the set up of the system). In practice a TDD simulation presumes that information about the local porosities and the apparent diffusion coefficients are available. With such information the transition probability for each jump can be determined using Eq. (4.6). After that a random number was selected to determine the jump direction based on these transition probabilities. Another random number was used for setting the transition time given by Eq (4.8). This procedure was repeated for each particle until a preset total diffusion time was elapsed.

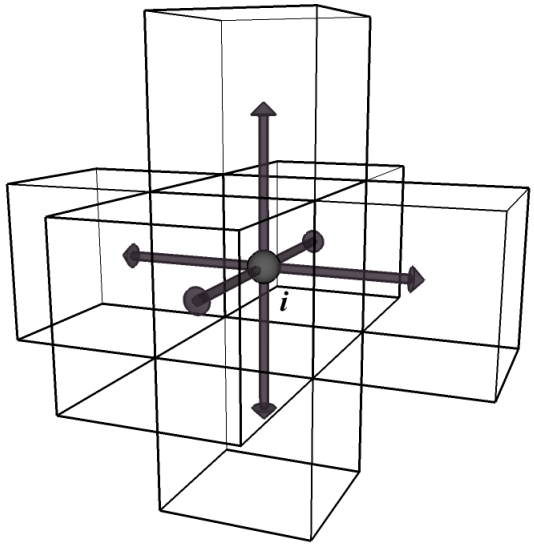

Figure 4.1. *Possible jumps in a 3D cubic lattice of a particle in voxel i. At each simulation step the particle is forced to jump to one of the neighbouring voxels. The transition time and transition probability of the jump were defined by Eq. (4.8) and Eq. (4.6), respectively.*

In the simulations 3D grayscale images were used as the simulation geometries, in which voxels formed a cubic simulation grid. For a particle at voxel i all the possible jumps are illustrated in Fig. 4.1 in the case of a cubic lattice. In a cubic lattice calculation of parameters L_{ij}, A_{ij}, and V_i becomes trivial along with the known voxel size. In practice, a 3D grayscale image was provided for the simulation program. In the image each component was coloured with a unique gray-scale value which was linked to its porosity and diffusion coefficient.

4.2 Validation of the TDD method

The TDD method was validated in 3D using three different systems: 1. Diffusion in a homogeneous slab was simulated, and compared the result with an analytical solution of the corresponding diffusion equation. 2. Diffusion through a homogeneous wall of infinitely long hollow cylinder was simulated, and compared the result with a numerical solution of the related diffusion equation. 3. Diffusion was simulated in a homogeneous sample constructed according to a measurement set up (see Fig. 4.4), and the results were compared with experimental data of a corresponding measurement.

Validation simulations in the homogeneous slab were performed as in-diffusion simulations in which there was a constant particle concentration, C_0, of the tracer at one face of the sample, and the tracer was let to diffuse through that face into the sample. Concentration profiles were determined as particle distributions as a function of intrusion depth. The total simulation time was chosen so that tracer particles did not appreciably reach the opposite face of the sample, which allowed fitting of the tracer distributions by a semi-infinite approximation of the solution to the corresponding diffusion equation [111]:

$$C = C_0 - C_0 erf \frac{x}{\sqrt{4D_a t}}, \tag{4.9}$$

where C_0 is the particle concentration on the entrance face, x the distance from the entrance surface, and t the diffusion time.

These validation simulations were performed in sample of 200×200×200 voxels with a voxel size of 90 μm. In the simulations various values, from $9.0 \cdot 10^{-13}$ to $2.0 \cdot 10^{-9}$ m^2/s, for the apparent diffusion coefficient (D_a) of the sample were used, and the simulated curves were fitted by Eq. (4.9) with D_a as the fitting parameter. These results indicated that the value of the apparent diffusion coefficient was accurately reproduced by the simulations. In Fig. 4.2 an in-diffusion profile is shown for an apparent diffusion coefficient of $2.5 \cdot 10^{-10}$ m^2/s and diffusion time of 0.5 d.

In the second validation case diffusion through the homogeneous wall of an infinitely long hollow cylinder was simulated. The diffusion process was initiated by placing an initial tracer concentration (C_0) in the central hole, and the tracer was then let to diffuse through the porous wall to the space surrounding the cylinder. The simulated breakthrough curve was compared with that of a numerically solved partial differential equation that describes the same diffusion problem. In the mathematical treatment it was assumed that the tracer migrates radially through the wall only by diffusion, and that the tracer concentrations in the central hole and around the cylinder were well mixed. In the present case it is beneficial to use the diffusion equation in cylindrical

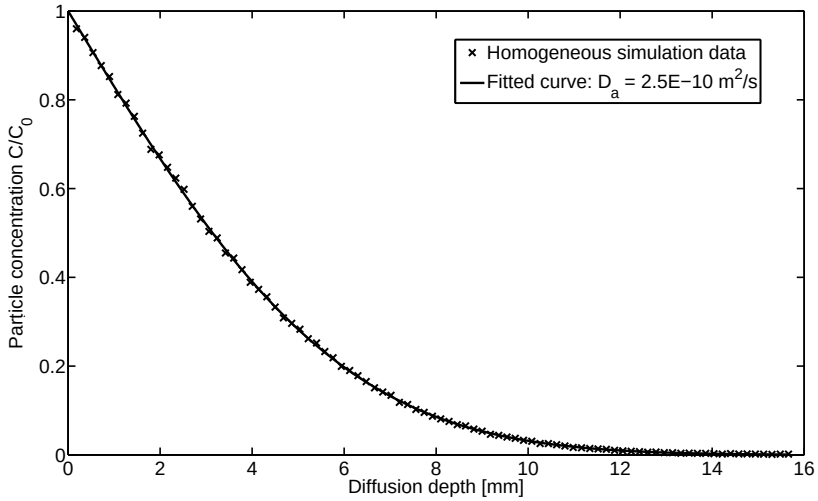

Figure 4.2. *Validation of the TDD method by an in-diffusion simulation in a homogeneous slab. A curve fitted (solid line) to simulated in-diffusion profile (markers) reproduces exactly the set value of the diffusion coefficient. Here the apparent diffusion coefficient is* $2.5 \cdot 10^{-10}$ m^2/s.

coordinates [111],

$$\frac{\partial^2 C(r,t)}{\partial r^2} + \frac{1}{r}\frac{\partial C(r,t)}{\partial r}) = \frac{1}{D_a}\frac{\partial C(r,t)}{\partial t}, \tag{4.10}$$

where $C(r,t)$ is the concentration of the tracer inside the wall as a function of radius (r) and time (t). The boundary and initial conditions can now be expressed in the form

$$\begin{aligned} D_a \frac{\partial C(r_1,t)}{\partial r} &= \frac{V_1}{\epsilon A_1}\frac{\partial C(r_1,t)}{\partial t} \\ D_a \frac{\partial C(r_2,t)}{\partial r} &= -\frac{V_2}{\epsilon A_2}\frac{\partial C(r_2,t)}{\partial t} \\ C(r,0) &= \begin{cases} C_0, & r = r_1 \\ \\ 0, & r_1 < r \leq r_2 \end{cases}, \end{aligned} \tag{4.11}$$

where V is the volume of the chamber per unit length, ϵ the porosity of the wall, and A the area of the surface per unit length through which diffusion takes place. Subscript 1 refers to the central hole and 2 to the surrounding space. Here the cross-sectional dimensions of the cylinder were comparable to the ones in the measurement system described below (see Fig. 4.4).

Simulations were performed in a sample of 190×190×10 voxels with a voxel size of 0.5 mm and a total diffusion time of 80 d. Periodic boundary conditions at the edges were imposed, which allowed simulation of diffusion in an infinitely long sample.

This was also assumed in the diffusion equation, Eq. (4.10), when making there the approximation of 1D radial diffusion. Tracer particles were placed randomly in the central cavity in the beginning of the simulation, and the tracer concentration in the surrounding chamber was measured continuously. The porosity and diffusion coefficient in the central hole and surrounding space was set to 100% and $2.2 \cdot 10^{-9}$ m^2/s, respectively. Various porosities and apparent diffusion coefficients were used for the sample in order to compare the simulated through diffusion curves with the numerically solved ones. It was found that TDD simulations exactly produce the through diffusion curve given by a numerical solution of the diffusion equation. In Fig. 4.3 a through diffusion curve is shown in the case when the porosity and apparent diffusion coefficient of the sample were set to 11% and $2.9 \cdot 10^{-10}$ m^2/s, respectively.

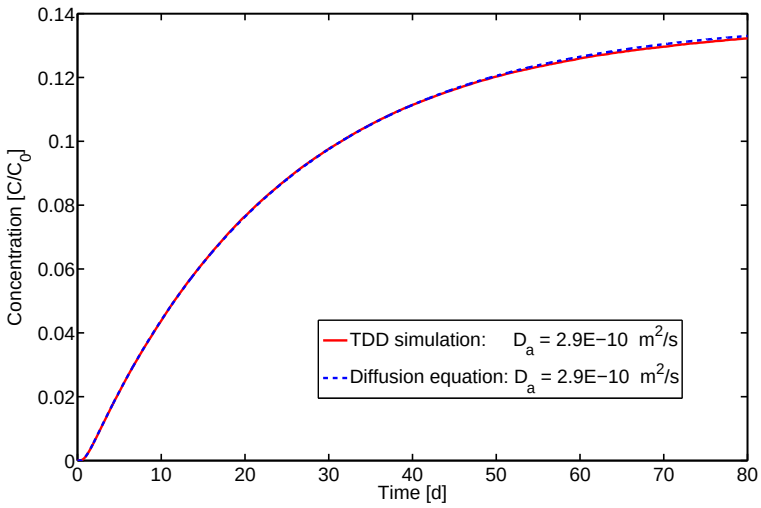

Figure 4.3. *The breakthrough curve of a TDD simulation and a numerical solution of the diffusion equation for diffusion through a homogeneous wall of an infinitely long hollow cylindrical sample. The simulated (red) curve agrees exactly with the one determined by a numerical solution of the diffusion equation (blue curve). Here the porosity was set to 11% and the apparent diffusion coefficient to* $2.9 \cdot 10^{-10}$ m^2/s.

Finally, for further validation, a relatively simple through diffusion type of measurement system was constructed (see Fig. 4.4). It consisted of a hollow cylindrical rock sample of Sievi altered tonalite with a bored central cavity. This sample was placed in a chamber. Experiment was carried out in water phase such that tritiated water (HTO) was used as the tracer and was inserted into the central cavity. HTO concentration was then monitored in the surrounding the chamber until a near equilibrium was reached after 76 days. A more detailed description of the measurement is found in Appendix V.

Corresponding simulations were performed in a sample of 166×166×108 voxels with a voxel size of 0.5 mm and a total diffusion time of 80 d. In the simulations the

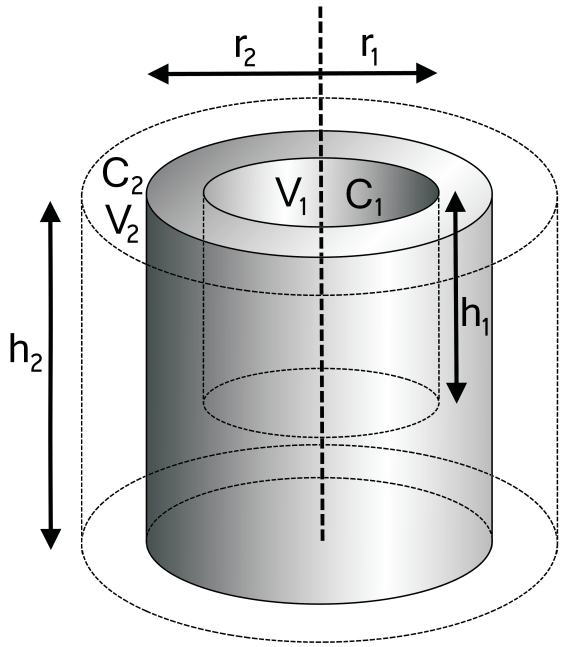

Figure 4.4. *A schematic layout of a measurement setup for validation of the used simulation method. The setup consists of a hollow rock cylinder with inner radius r_1 (15.1 mm), outer radius r_2 (28.0 mm), height of the central cavity h_1 (33.1 mm), height of the sample h_2 (53.1 mm), volume of the central cavity V_1 (25 ml), and volume of the surrounding chamber V_2 (150 ml). Initial input concentration ($C_1(t = 0) = C_0$) of the tracer was known and its concentration (C_2) in the surrounding chamber was continuously measured.*

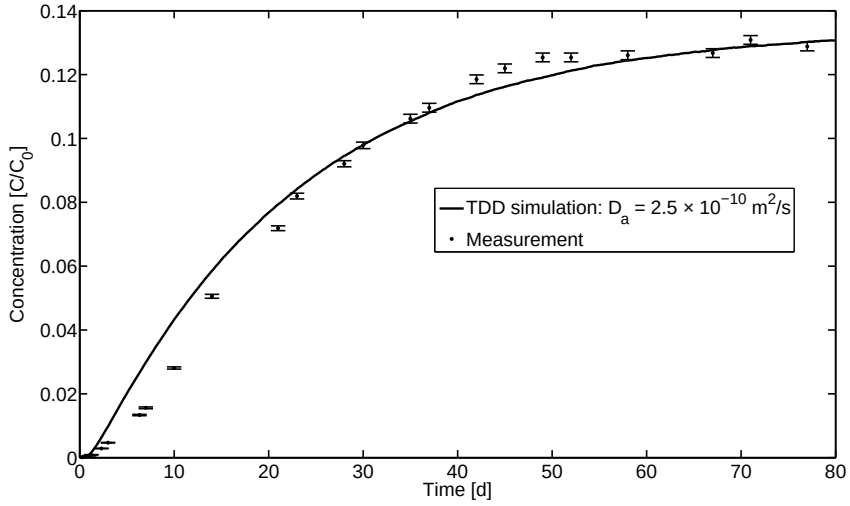

Figure 4.5. *Validation of the TDD method by a through diffusion measurement of HTO. Best agreement between the measured data points and TDD simulations (solid line) was found for an apparent diffusion coefficient of* $2.5 \cdot 10^{-10}$ m^2/s.

porosity and diffusion coefficient in the central cavity and surrounding chamber were set to 100% and $2.236 \cdot 10^{-9}$ m^2/s, respectively, the latter of which is the diffusion coefficient of HTO in water at 25 °C [141]. As for the porosity of rock matrix, a previously measured porosity of 11% was used (see Sec. 3.3) and the apparent diffusion coefficient was varied in order to find the best possible agreement with measured data using least-square fitting. Otherwise, simulations were prepared as in the case of the infinite hollow cylinder. The best possible agreement between measurement and simulations was found when an apparent diffusion coefficient of $2.5 \cdot 10^{-10}$ m^2/s was used (see Fig. 4.5). It is evident from these results that the sample cannot very accurately be described as one with homogeneous porosity, and that heterogeneity of rock plays a role in the migration of the tracer. The determined value is about an order of magnitude higher than the values previously reported for altered Sievi tonalite [32]. This is due to the fact that the sample used in the present analysis was more altered and had about twice as high a porosity as in the samples used in the earlier studies. Nevertheless, as the apparent diffusion coefficient determined was about an order of magnitude lower than that for HTO in water, it is probably quite a reasonable estimate for the true value.

In addition, the results of TDD simulations and discrete-time random-walk simulations [142] were compared in an artificial 3D porous medium formed by randomly placed impermeable spheres. The results of these simulations were identical and are found in Appendix V. Previously a similar comparison of the TDD method with a classical random walker has also been done for 2D porous samples [104].

4.3 The effect of heterogeneous porosity to diffusion coefficient

Validation of the TDD model was followed by analysis of the effect of heterogeneous porosity on the diffusion coefficient in the Sievi sample of altered tonalite, for which the heterogeneous (3D) distribution of porosity was determined in Sec. 3.3. In the simulations, a sample of Sievi tonalite comprising 200×200×200 voxels sized sample of Sievi tonalite was used (see Fig. 4.6). The original voxel size was increased from 14.4 to 90 μm, since, according the discretization study, it did not affect the results in the present case and the simulation times were reduced significantly.

A secondary aim for validating the TDD method by the diffusion experiment of the previous Section was to provide a global value for the apparent diffusion coefficient in Sievi tonalite of HTO molecules. The determined value was used in this analysis as the apparent diffusion coefficient ($D_a = 2.5 \cdot 10^{-10}$ m^2/s) for the rock matrix. As for

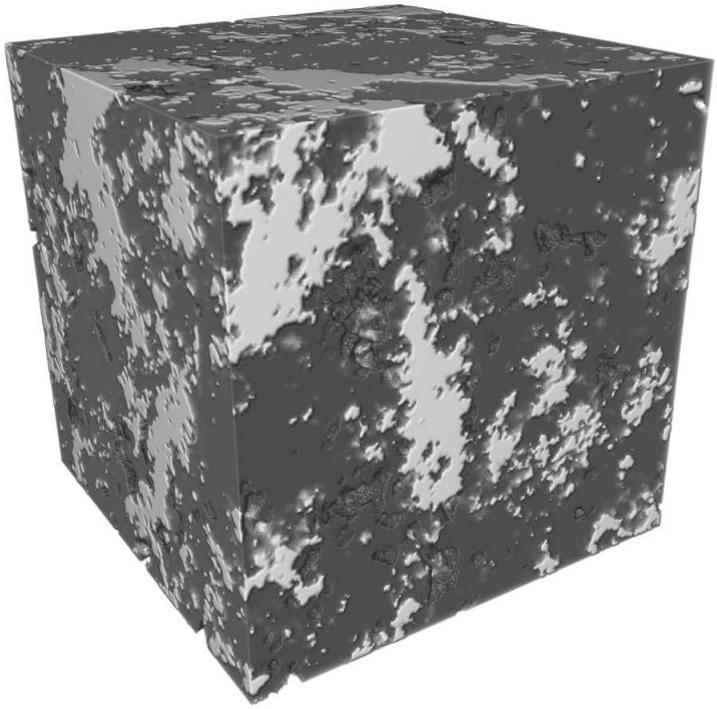

Figure 4.6. *The sample of Sievi tonalite (16×16×16 mm^3) used to study the effect of heterogeneous porosity using the TDD method. This sample consists of pores (black), altered feldspar (dark gray), altered mica (light gray) and accessory minerals (white).*

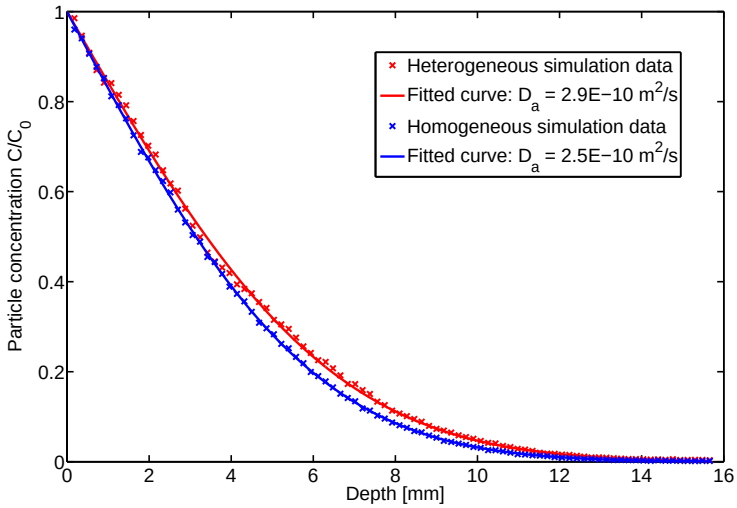

Figure 4.7. *In-diffusion profiles for Sievi tonalite assuming a heterogeneous (blue) and homogeneous (red) porosity in the rock matrix. Markers denote the simulated in-diffusion profiles and continuous lines show least-squares fits to them by Eq. (4.9).*

porosity, the previously determined values for the different mineral components were used (4.5% altered feldspar, 8.6% altered mica and 0% accessory minerals, see Sec. 3.3) so as to model the heterogeneous distribution of porosity in altered Sievi tonalite. For the pore space the diffusion coefficient and porosity were set to $2.2 \cdot 10^{-9}$ m^2/s and 100%, respectively. Otherwise the simulations were performed similarly to the first validation simulation, as in-diffusion simulations in order to compare the resulting in-diffusion profiles with the one produced by a homogeneous distribution of porosity (see Fig. 4.2).

Results of these simulations and the effect of heterogeneous porosity in Sievi tonalite is shown in Fig. 4.7. It was found that the apparent diffusion coefficient increased from $2.5 \cdot 10^{-10}$ to $2.9 \cdot 10^{-10}$ m^2/s when the heterogeneity of porosity was taken into account. In other words, in the case of Sievi tonalite the diffusivity is increased by 16% because of heterogeneous porosity. Heterogeneity seems thus to be fairly relevant.

Finally, the relative contributions of different components (pores and minerals) of Sievi tonalite to the apparent diffusion coefficient were estimated. These simulations were done for the same sample of Sievi tonalite (see Fig. 4.6) as when studying the effect of heterogeneous porosity, except that now the apparent diffusion coefficient of one or two components at a time was set to zero. Hence, the sensitivity of diffusion to these components was estimated. The results of these simulations are shown in Fig. 4.8. For comparison, the case when all components are present is also shown. As expected, the dominant component (altered feldspar) also dominates the bulk diffusion behaviour. Removal of diffusivity in altered feldspar reduced the apparent diffusion coefficient by 76%, and removal of diffusivity in large pores and mica simultaneously reduced the apparent diffusion coefficient by 48%. As for large pores and altered mica, their contributions to the global diffusion coefficient were found to be very similar and smaller than the contribution of feldspar. It was also found that these results are not only related to the connectivities of different phases, but also to their porosities.

A possible presence of diffusion anisotropy was investigated by changing the intrusion face of the tracer. No diffusion anisotropy was found for this sample. This result is in agreement with the visual observation that there is no mineral orientation in the sample.

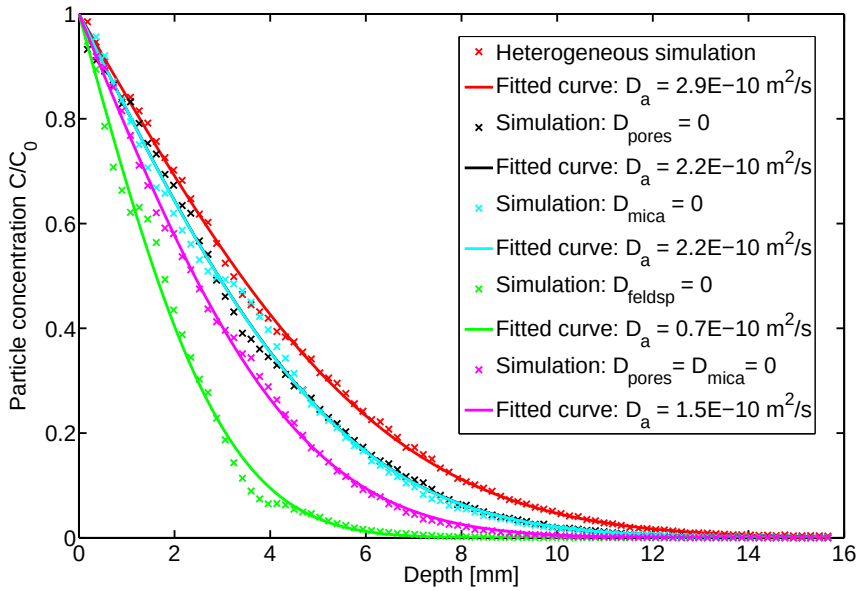

Figure 4.8. *Contributions of different components in Sievi tonalite to the in-diffusion profile of the tracer. Setting the apparent diffusion coefficient of one or two components to zero decreased the original penetration profile (red). Removal of the diffusivity of feldspar (green) had the largest contribution to the penetration profile, while removal of the diffusivity of open pores (black) and mica (blue) both made a smaller contribution. The dominant component (feldspar) explained alone 52% of the global diffusion coefficient (magenta).*

Chapter 5

Conclusions and outlook

The objectives of this Thesis were to construct characterization methods for porous rock and analysis methods for molecular diffusion in such materials with respect to long term safety of nuclear waste disposal. The final goal was to combine these two objectives and to model diffusion in a realistic presentation of tight crystalline rock. To this end the pore structures were characterized by X-μCT and the ^{14}C-PMMA method, and analytical and simulation techniques were developed for matrix diffusion. Diffusion measurements were done to validate modeling and to determine the diffusion coefficients needed in the simulations. Mathematical methods were also used to illustrate effects of matrix diffusion in varying situations.

A semi-analytic solution of the advection-matrix diffusion model was successfully validated by laboratory scale measurements in which a tracer input was advected past a porous matrix. First of all the measurement system was used to validate the solution for a delta-pulse input in the case of matrix of finite depth. The effect of finite matrix was demonstrated by varying advection in the flow channel, and was observed clearly in the late time behaviour of the breakthrough curve. For decreased advection the amount of tracer molecules that were reflected from the back wall of the porous matrix was increased, and a hump appeared in the tail of the breakthrough curve. Such measurements were also used to validate the solution in a situation in which the tracer undergoing matrix diffusion already appears in the porous matrix. From the nuclear waste disposal point of view this kind of situation may occur when an ice age is drawing back and fresh melting water is getting in touch with the repository system. In our measurements the resulting breakthrough curves were divided into two components, one from input and another from the tracer initially in the system. The main advantage of this approach is that an arbitrary input and initial conditions can be applied when analyzing, e.g., in situ bedrock experiments in which these conditions may be difficult to control. In both validation cases the apparent diffusion coefficients

determined by fitting corresponded exactly to the ones determined by other means [113]. Furthermore, the advection-matrix diffusion models considered included longitudinal diffusion and Taylor dispersion of the tracer in the flow channel, as well as a varying aperture of the flow channel. However, in the present measurement system the effect of the former phenomena were found to be negligible. It was demonstrated that the effect of varying aperture can be accounted for by simply using its average value in the expression for the breakthrough curve (details are shown in Appendix III). In general, the experimental system introduced was found to be a versatile tool for demonstrating the effects of relevant diffusion processes that appear in these kinds of system.

The characterization methods combining X-μCT and the ^{14}C-PMMA method were found to be applicable when studying the structure of geological materials. First of all, abundances of different minerals, large-aperture porosities and pore connectivities were determined from X-μCT reconstructions of varying voxel size. In the case of altered Sievi tonalite, it was found that porosity, abundance of accessory minerals and connectivity increased with decreasing voxel size, and we could conclude that a significant amount of pores, accessory mineral grains and pore throats has a size within the used range of voxel sizes. The abundances of altered feldspar and mica did not change significantly with changing voxel size. In addition, X-μCT reconstructions were used to determine the pore size and porosity distributions for detected pores. These distributions were found to be similar to log-normal distributions which are often observed in nature. If needed, similar analysis could also be done of mineral grains. The ^{14}C-PMMA method, followed by mineral staining and segmentation, was applied to resolve the porosity distributions of 2D rock surfaces and intragranular porosities of different mineral groups. Finally, 3D porosity maps were constructed by replacing the minerals of tomographic reconstructions by the intragranular porosities evaluated by the ^{14}C-PMMA method. In addition, SEM and argon pycnometry were found to offer valuable additional information about the pore structure and mineralogy, and more importantly with these methods we could verify results of X-μCT and the ^{14}C-PMMA method with regard to porosity and pore sizes.

It was demonstrated above that the TDD method can be used to model diffusion processes in rock. First of all we successfully validated the method in three different cases. The results of TDD simulations were: 1. They could exactly reproduce the results found by solving the corresponding diffusion equation in the case of a cubic sample and an infinitely long hollow cylinder. 2. They were found to compare well with those of a through diffusion laboratory experiment. 3. They were found to be equivalent to those of DTRW simulations for porous samples made of randomly placed overlapping spheres (results shown in Appendix V). More importantly, TDD simulations were used to study the effect of heterogeneous distribution of porosity on the diffusion process in rock by applying one of the porosity maps constructed

by combination of X-μCT and the ^{14}C-PMMA method. In the case considered a clear influence on the diffusion coefficient of heterogeneous porosity was indeed found. Comparison with simulations on a homogeneous sample revealed that heterogeneity increased the apparent diffusion coefficient by 16%. TDD simulations were also used to estimate the contribution of different components to the diffusion coefficient. As expected, contribution of the main component (altered feldspar) was dominating. However, the large pores (pores resolved by X-μCT) played a significant role in the diffusion process. In addition, TDD simulations were used test directional dependence which was not, however, found in the present case. Nevertheless, in rock with clear foliation anisotropic diffusion will certainly appear.

In conclusion, the developed analysis methods offer an effective combination of tools for detailed characterization of the structure of porous rock and for studying diffusive transport in it. It was shown that effects seen in the performed matrix diffusion measurements can fully be explained by semi-analytical solutions of the advection-matrix diffusion model. Furthermore, such solutions can be used to analyze, interpret, and predict the results of a wide range of matrix diffusion measurements. It was demonstrated that combinations of different analysis methods can be used to infer novel structural information about geological materials, which can be used to improve, e.g., our understanding of alteration processes and their outcomes. The 3D porosity map introduced here could be constructed even more realistically using the porosity distribution data of each separate mineral found by the ^{14}C-PMMA method, and generating equivalent porosity distributions in the 3D representation of porosity. This further improvement would make the diffusion environment even more realistic for e.g. TDD simulations. It was shown that TDD simulations can be used to estimate the effect of heterogeneity and to analyze results of diffusion measurements. Especially when analytic solutions are not available, simulations offer a valuable tool for studying diffusion. The TDD method could be developed further by implementing in it adsorption-desorption processes and the possibility of advection. These improvements would significantly increase applications of the method since in many diffusion processes adsorption plays an important role, and part of the solute transport may be advective, as in the measurements of Sec. 2.2. Here, in this Thesis, altered Sievi tonalite was used in the structure characterization and TDD simulation studies. However, the methods introduced here could also be used in a larger-scale research of other porous rocks and materials.

Bibliography

[1] C. McCombie. Nuclear waste management worldwide. *Phys. Today*, 50(6):56–62, 1997.

[2] N.T. Rempe. Permanent underground repositories for radioactive waste. *Prog. Nucl. Energ.*, 49(5):365–374, 2007.

[3] J.-S. Kim, S.-K. Kwon, M. Sanchez, and G.-C. Cho. Geological storage of high level nuclear waste. *KSCE J. Civ. Eng.*, 15(4):721–737, 2011.

[4] G. Bäckblom. Progress towards a deep repository for spent nuclear fuel in Sweden. *J. Nucl. Sci. Technol.*, 35(9):623–630, 1998.

[5] T. McEven and T. Äikäs. The site selection process for a spent fuel repository in Finland - summary report. Posiva Report 2000-15, Posiva Oy, 2000.

[6] A.G. Milnes, M.B. Stephens, C.-H. Wahlgren, and L. Wikström. Geoscience and high-level nuclear waste disposal: the Nordic scene. *Episodes*, 31:168–175, 2008.

[7] M.I. Sheppard, B.D. Amiro, P.A. Davis, and R. Zach. Continental glaciation and nuclear fuel waste disposal: Canada's approach and assessment of the impact on nuclide transport through the biosphere. *Ecol. Model.*, 78:249–265, 1995.

[8] L. Forsström. Future glaciation in Fennoscandia. Posiva Report 99-30, Posiva Oy, 1999.

[9] K.L. Hutri and J. Antikainen. Modelling of the bedrock response to glacial loading at the Olkiluoto site, Finland. *Eng. Geol.*, 67(1-2):39–49, 2002.

[10] T. Vieno and A. Ikonen. Plan for safety case of spent fuel repository at Olkiluoto. Posiva Report 2005-01s, Posiva Oy, 2005.

[11] I. Neretnieks. Diffusion in the rock matrix: An important factor in radionuclide retardation? *J. Geophys. Res.*, 85(B8):4379–4397, 1980.

[12] M. Mazurek, W.R. Alexander, and A.B. MacKenzie. Contaminant retardation in fractured shales: matrix diffusion and redox front entrapment. *J. Cont. Hydrol.*, 21(1-4):71–84, 1996.

[13] S. Xu, A. Wörman, and B. Dverstorp. Heterogeneous matrix diffusion in crystalline rock - implications for geosphere retardation of migrating radionuclides. *J. Cont. Hydrol.*, 47(2-4):365–378, 2001.

[14] J. Liu, M. Löfgren, and I. Neretnieks. Data and uncertainty assessment: Matrix diffusivity and porosity in situ. Tecnical Report R-06-111, SKB, 2006.

[15] S.S.D. Foster. The chalk groundwater tritium anomaly - A possible explanation. *J. Hydrol.*, 25(1-2):159–165, 1975.

[16] D. Norton and R. Knapp. Transport phenomena in hydrothermal systems: the nature of porosity. *Am. J. Sci.*, 277:913–936, 1977.

[17] W.W. Wood, T.F. Kraemer, and P.P. Hearn. Intragranular diffusion: an important mechanism influencing solute transport in classic aquifers? *Science*, 247:1569–1572, 1990.

[18] J. Guimera and J. Carrera. A comparison of hydraulic and transport parameters measured in low-permeability fractured media. *J. Cont. Hydrol.*, 41(3-4):261–281, 2000.

[19] K. Skagius and I. Neretnieks. Porosities and diffusivities of some nonsorbing species in crystalline rocks. *Water Resour. Res.*, 22(3):389–398, 1986.

[20] A.M. Shapiro. Effective matrix diffusion in kilometer-scale transport in fractured crystalline rock. *Water Resour. Res.*, 37(3):507–522, 2001.

[21] I. Neretnieks. A stochastic multi-channel model for solute transport - analysis of tracer tests in fractured rock. *J. Cont. Hydrol.*, 55(3-4):175–211, 2002.

[22] J. Hartikainen, K. Hartikainen, A. Hautojärvi, K. Kuoppamäki, and J. Timonen. Helium gas methods for rock characteristics and matrix diffusion. Posiva Report 96-22, Posiva Oy, 1996.

[23] Y. Ohlsson, M. Löfgren, and I. Neretnieks. Rock matrix diffusivity determinations by in-situ electrical conductivity measurements. *J. Cont. Hydrol.*, 47(2-4):117–125, 2001.

[24] A. Möri, W.R. Alexander, H. Geckeis, W. Hauser, T. Schäfer, J. Eikenberg, T. Fierz, C. Degueldre, and T. Missana. The colloid and radionuclide retardation experiment at the Grimsel Test Site: influence of bentonite colloids on radionuclide migration in a fractured rock. *Colloid. Surface. A*, 217(1-3):33–47, 2003.

[25] P. Vilks, J.J. Cramer, M. Jensen, N.H. Miller, H.G. Miller, and F.W. Stanchell. In situ diffusion experiment in granite: Phase I. *J. Cont. Hydrol.*, 61(1-4):191–202, 2003.

[26] P. Aalto, I. Aaltonen, H. Ahokas, J. Andersson, M. Hakala, P. Hellä, J. Hudson, E. Johansson, K. Kemppainen, L. Koskinen, M. Laaksoharju, M. Lahti, S. Lindgren, A. Mustonen, K. Pedersen, P. Pitkänen, A. Poteri, M. Snellman, and M. Ylä-Mella. Programme for repository host rock characterisation in the ONKALO (ReRoC). Working Report 2009-31, Posiva Oy, 2009.

[27] D. Hodgkinson, H. Benabderrahmane, M. Elert, A. Hautojärvi, J. Selroos, Y. Tanaka, and M. Uchida. An overview of Task 6 of the Äspö Task Force: modelling groundwater and solute transport: improved understanding of radionuclide transport in fractured rock. *Hydrogeol. J.*, 17(5):1035–1049, 2009.

[28] L. Moreno, I. Neretnieks, and T. Eriksen. Analysis of some laboratory tracer runs in natural fissures. *Water Resour. Res.*, 21(7):951–958, 1985.

[29] P. Hölttä, A. Hautojärvi, and M. Hakanen. Transport and retardation of nonsorbing radionuclides in crystalline rock fractures. *Radiochim. Acta*, 58/59:285–290, 1992.

[30] K. Hartikainen, A. Hautojarvi, H. Pietarila, and J. Timonen. Diffusion measurements on crystalline rock matrix. In T. Murakami and R. Ewing, editors, *MRS proceedings: Scientific Basis for Nuclear Waste Management XVIII*, pages 435–440, Pittsburgh, 1995. MRS.

[31] P. Hölttä, M. Siitari-Kauppi, M. Hakanen, T. Huitti, A. Hautojärvi, and A. Lindberg. Radionuclide transport and retardation in rock fracture and crushed rock column experiments. *J. Cont. Hydrol.*, 26(1-4):135–145, 1997.

[32] M. Siitari-Kauppi, A. Lindberg, K.-H. Hellmuth, J. Timonen, K. Väätäinen, J. Hartikainen, and K. Hartikainen. The effect of microscale pore structure on matrix diffusion - a site-specific study on tonalite. *J. Cont. Hydrol.*, 26(1-4):147–158, 1997.

[33] D.H. Tang, E.O. Frind, and E.A. Sudicky. Contaminant transport in fractured porous media: Analytical solutions for a single fracture. *Water Resour. Res.*, 17(3):555–564, 1981.

[34] C.A. Kennedy and W. Lennox. A control volume model of solute transport in a single fracture. *Water Resour. Res.*, 31(2):313–322, 1995.

[35] J. Hadermann and W. Heer. The Grimsel (Switzerland) migration experiment: integrating field experiments, laboratory investigations and modelling. *J. Cont. Hydrol.*, 21(1-4):87–100, 1996.

[36] R. Chittaranjan, T.R. Ellsworth, A.J. Valocchi, and C.W. Boast. An improved dual porosity model for chemical transport in macroporous soils. *J. Hydrol.*, 193(1-4):270–293, 1997.

[37] V. Cvetkovic, J.-O. Selroos, and H. Cheng. Transport of reactive tracers in rock fractures. *J. Fluid Mech.*, 378:335–356, 1999.

[38] C. Doughty. Investigation of conceptual and numerical approaches for evaluating moisture, gas, chemical, and heat transport in fractured unsaturated rock. *J. Cont. Hydrol.*, 38(1-3):69–106, 1999.

[39] S. Painter, V. Cvetkovic, J. Mancillas, and O. Pensado. Time domain particle tracking methods for simulating transport with retention and first-order transformation. *Water Resour. Res.*, 44, 2008. W01406.

[40] F. Delay, A. Kaczmaryk, and P. Ackerer. Inversion of a Lagrangian time domain random walk (TDRW) approach to one-dimensional transport by derivation of the analytical sensitivities to parameters. *Adv. Water Resour.*, 31(3):484–502, 2008.

[41] C.I. McDermott, R. Walsh, R. Mettier, G. Kosakowski, and O. Kolditz. Hybrid analytical and finite element numerical modeling of mass and heat transport in fractured rocks with matrix diffusion. *Comput. Geosci.*, 13:349–361, 2009.

[42] D.A. Lever, M.H. Bradbury, and S.J. Hamingway. The effect of dead-end porosity on rock-matrix diffusion. *J. Hydrol.*, 80(1-2):45–76, 1985.

[43] M.H. Bradbury and A. Green. Investigations into the factors influencing long range matrix diffusion rates and pore space accessibility at depth in granite. *J. Hydrol.*, 89(1-2):123–139, 1986.

[44] N. Epstein. On tortuosity and the tortuosity factor in flow and diffusion through porous media. *Chem. Eng. Sci.*, 44(3):777–779, 1989.

[45] E.E. Petersen. Diffusion in a pore of varying cross section. *AIChE J.*, 4(3):343–345, 1958.

[46] A.S. Michaels. Diffusion in a pore of irregular cross section - a simplified treatment. *AIChE J.*, 5(2):270–271, 1959.

[47] J. Van Brakel and P.M. Heertjes. Analysis of diffusion in macroporous media in terms of a porosity, a tortuosity and a constrictivity factor. *Int. J. Heat Mass Tran.*, 17(9):1093–1103, 1974.

[48] J. Bear. *Dynamics of fluids in porous media.* Dover Publications, New York, 1972.

[49] F.A.L. Dullien. *Porous media: Fluid transport and pore structure*. Academic Press, San Diego, 1979.

[50] M.B. Clennell. Tortuosity: a guide through the maze. *Geol. Soc. Spec. Publ.*, 122:299–344, 1997.

[51] G.N. Hounsfield. Method and aparatus for measuring X- and γ -radiation absorption or transmission at plural angles and analyzing the data, us patent 3, 778, 614, 1970.

[52] G.N. Hounsfield. Computerized transverse axial scanning (tomography): Part 1. Description of the system. *Brit. J. Radiol.*, 46:1016–1022, 1973.

[53] R.A. Ketcham and W.D. Carlson. Acquisition, optimization and interpretation of X-ray computed tomographic imagery: Applications to the geosciences. *Comput. Geosci.*, 27(4):381–400, 2001.

[54] W. D. Carlson, T. Rowe, R.A. Ketcham, and M.W. Colbert. Applications of high-resolution X-ray computed tomography in petrology, meteoritics and palaeontology. *Geol. Soc. Spec. Publ.*, 215:7–22, 2003.

[55] V. Cnudde, B. Masschaele, M. Dierick, J. Vlassenbroeck, L. Van Hoorebeke, and P. Jacobs. Recent progress in X-ray CT as a geosciences tool. *Appl. Geochem.*, 21(5):826–832, 2006.

[56] B. Haubitz, M. Prokop, W. Dohring, J.H. Ostrom, and P. Wellnhofer. Computed tomography of Archaeopteryx. *Paleobiology*, 14(2):206–213, 1988.

[57] R.S. Tykoski, T.B. Rowe, R.A. Ketcham, and M.W. Colbert. Calsoyasuchus valliceps, a new crocodyliform from the Early Jurassic Kayenta Formation of Arizona. *J. Vertebr. Paleontol.*, 22(3):593–611, 2002.

[58] M. Van Geet, D. Lagrou, and R. Swennen. Porosity measurements of sedimentary rocks by means of microfocus X-ray computed tomography. *Geol. Soc. Spec. Publ.*, 215(1):51–60, 2003.

[59] V. Cnudde, M. Boone, J. Dewanckele, M. Dierick, L. Van Hoorebeke, and P. Jacobs. 3D characterization of sandstone by means of X-ray computed tomography. *Geosphere*, 7(1):54–61, 2011.

[60] M. Van Geet, R. Swennen, and M. Wevers. Towards 3-D petrography: Application of microfocus computer tomography in geological science. *Comput. Geosci.*, 27(9):1091–1099, 2001.

[61] S. Crestana, S. Mascarenhas, and R.S. Pozzi-Mucelli. Static and dynamic three-dimensional studies of water in soil using computed tomographic scanning. *Soil Sci.*, 140(5):326–332, 1985.

[62] I.A. Taina, R.J. Heck, and T.R. Elliot. Application of X-ray computed tomography to soil science: A literature review. *Can. J. Soil. Sci.*, 88(1):1–19, 2008.

[63] S.Y. Wang, Y.B. Huang, V. Pereira, and C.C. Gryte. Application of computed tomography to oil recovery from porous media. *Appl. Opt.*, 24(23):4021–4027, 1985.

[64] S. L. Wellington and H.J. Vinegar. X-ray computerized tomography. *J. Pet. Technol.*, 39(8):885–898, 1987.

[65] S. Akin and A.R. Kovscek. Computed tomography in petroleum engineering research. *Geol. Soc. Spec. Publ.*, 215:23–38, 2003.

[66] H.J. Vinegar and S.L. Wellington. Tomographic imaging of three-phase flow experiments. *Rev. Sci. Instrum.*, 58(1):96–107, 1987.

[67] J.-F. Thovert, F. Yousefian, P. Spanne, C.G. Jacquin, and P.M. Adler. Grain reconstruction of porous media: Application to a low-porosity Fontainebleau sandstone. *Phys. Rew. E*, 63(6), 2001. 061307.

[68] L. Farber, G. Tardos, and J.N. Michaels. Use of X-ray tomography to study the porosity and morphology of granules. *Powder Technol.*, 132(1):57–63, 2003.

[69] C.J. Gommes, A.-J. Bons, S. Blacher, J.H. Dunsmuir, and A.H. Tsou. Practical methods for measuring the tortuosity of porous materials from binary or gray-tone tomographic reconstructions. *AIChE J.*, 55(8):2000–2012, 2009.

[70] V. Cnudde, J. Dewanckele, M. Boone, T. de Kock, M. Boone, L. Brabant, M. Dusar, M. de Ceukelaire, H. de Clercq, R. Hayen, and P. Jacobs. High-resolution X-ray CT for 3D petrography of ferruginous sandstone for an investigation of building stone decay. *Microsc. Res. Techniq.*, 74(11):1006–1017, 2011.

[71] P. Gouze and L. Luquot. X-ray microtomography characterization of porosity, permeability and reactive surface changes during dissolution. *J. Cont. Hydrol.*, 120-121:45–55, 2011.

[72] F. Fusseis, K. Regenauer-Lieb, J. Liu, R.M. Hough, and F. De Carlo. Creep cavitation can establish a dynamic granular fluid pump in ductile shear zones. *Nature*, 459:974–977, 2009.

[73] P. Sardini, M. Siitari-Kauppi, D. Beaufort, and K.-H. Hellmuth. On the connected porosity of mineral aggregates in crystalline rocks. *Am. Mineral.*, 91(7):1069–1080, 2006.

[74] K.-H. Hellmuth, M. Siitari-Kauppi, and A. Lindberg. Applications of the carbon-14-polymethylmethacrylate PMMA impregnation method in studies on porosity and matrix diffusion. In C.G. Sombret, editor, *MRS proceedings: Scientific Basis for Nuclear Waste Management XV*, pages 649–656, Pittsburgh, 1992. MRS.

[75] K.-H. Hellmuth, M. Siitari-Kauppi, and A. Lindberg. Study of porosity and migration pathways in crystalline rock by impregnation with 14C-polymethylmethacrylate. *J. Cont. Hydrol.*, 13(1-4):403–418, 1993.

[76] K.-H. Hellmuth, S. Lukkarinen, and M. Siitari-Kauppi. Rock matrix studies with carbon-14-polymethylmethacrylate (PMMA): Method development and applications. *Isot. Environ. Healt S.*, 30(1):47–60, 1994.

[77] K.-H. Hellmuth, M. Siitari-Kauppi, P. Klobes, K. Meyer, and J. Goebbels. Imaging and analyzing rock porosity by autoradiography and Hg-porosimetry/X-ray computertomography - Applications. *Phys. Chem. Earth Pt. A*, 24(7):569–573, 1999.

[78] M. Siitari-Kauppi. *Development of 14C-polymethylmethacrylate method for the characterisation of low porosity media: Application to rocks in geological barriers of nuclear waste storage*. PhD thesis, University of Helsinki, 2002. Report Series in Radiochemistry 17.

[79] J.C. Robinet, P. Sardini, F. Delay, and K.-H. Hellmuth. The effect of rock matrix heterogeneities near fracture walls on the residence time distribution (RTD) of solutes. *Transport Porous Med.*, 72(3):393–408, 2008.

[80] D. Pret, S. Sammartino, D. Beaufort, M. Fialin, P. Sardini, P. Cosenza, and A. Meunier. A new method for quantitative petrography based on image processing of chemical element maps: Part II. Semi-quantitative porosity maps superimposed on mineral maps. *Am. Mineral.*, 95(10):1389–1398, 2010.

[81] E.D. Pittman and J.B. Thomas. Some applications of scanning electron microscopy to the study of reservoir rock. *J. Petrol. Technol.*, 31(11):1375–1380, 1979.

[82] G.E. Lloyd and M.G. Hall. Application of scanning electron microscopy to the study of deformed rocks. *Tectonophysics*, 78(1-4):687–698, 1981.

[83] D.J. Prior, P.W. Trimby, U.D. Weber, and D.J. Dingley. Orientation contrast imaging of microstructures in rocks using forescatter detectors in the scanning electron microscope. *Mineral. Mag.*, 60(6):859–869, 1996.

[84] S.J.B. Reed. *Electron microprobe analysis and scanning electron microscopy in geology*. Cambridge University Press, New York, 2005.

[85] M. Sahimi. *Flow and transport in porous media and fractured rock: From classical methods to modern approaches*. VCH, Weinheim, 1995.

[86] L. Moreno, B. Gylling, and I. Neretnieks. Solute transport in fractured media - the important mechanisms for performance assessment. *J. Cont. Hydrol.*, 25(3-4):283–298, 1997.

[87] M. L. Brusseau. The influence of solute size, pore water velocity, and intraparticle porosity on solute dispersion and transport in soil. *Water Resour. Res.*, 29(4):1071–1080, 1993.

[88] A.C. Bagtzoglou and D.D. Kim. Modeling contaminant transport at the pore-micropore interface. *Water Air Soil Poll.*, 6(1-2):207–225, 2006.

[89] L.R. Van Loon, J. Soler, W. Müller, and L. Bradbury. Anisotropic diffusion in layered argillaceous rocks: A case study with Opalinus Clay. *Environ. Sci. Technol.*, 38(21):5721–5728, 2004.

[90] E. Pankina, V. Rumynin, A. Nikulenkov, M. Glukhova, V. Epimakhov, S. Mysik, M. Baev, V. Kobekov, and V. Degtev. Anisotropy of clays in diffusion transport of radionuclides. *Radiochemistry*, 52(6):630–637, 2010.

[91] H. Scher and M. Lax. Stochastic transport in disordered solid. II. Impurity conduction. *Phys. Rev. B*, 7(10):4502–4519, 1973.

[92] B. Berkowitz, G. Kosakowski, G. Margolin, and H. Scher. Application of continuous time random walk theory to tracer test measurements in fractured and heterogeneous porous media. *Ground Water*, 39(4):593–604, 2001.

[93] N. Jeong, D.H. Choi, and C.-L. Lin. Estimation of thermal and mass diffusivity in a porous medium of complex structure using a lattice Boltzmann method. *Int. J. Heat Mass Tran.*, 51(15-16):3913–3923, 2008.

[94] Y.M. Xuan, K. Zhao, and Q. Li. Investigation on mass diffusion process in porous media based on Lattice Boltzmann method. *Heat Mass Transfer*, 46(10):1039–1051, 2010.

[95] J.M. Zalc, S.C. Reyes, and E. Iglesia. Monte-Carlo simulations of surface and gas phase diffusion in complex porous structures. *Chem. Eng. Sci.*, 58(20):4605–4617, 2003.

[96] Y. Nakashima, T. Nakanoa, K. Nakamuraa, K. Uesugib, A. Tsuchiyamac, and S. Ikedad. Three-dimensional diffusion of non-sorbing species in porous sandstone: Computer simulation based on X-ray microtomography using synchrotron radiation. *J. Cont. Hydrol.*, 74(1-4):253–264, 2004.

[97] M.E. Rhodes, B. Bijeljic, and M.J. Blunt. Pore-to-field simulation of single-phase transport using continuous time random walks. *Adv. Water Resour.*, 31(12):1527–1539, 2008.

[98] R. Mettier, G. Kosakowski, and O. Kolditz. Influence of small-scale heterogeneities on contaminant transport in fractured crystalline rock. *Ground Water*, 44(5):687–696, 2006.

[99] B. Berkowitz, H. Scher, and S.E. Silliman. Anomalous transport in laboratory-scale, heterogeneous porous media. *Water Resour. Res.*, 36(1):149–158, 2000.

[100] B. Berkowitz, A. Cortis, M. Dentz, and H. Scher. Modeling non-Fickian transport in geological formations as a continuous time random walk. *Rev. Geophys.*, 44, 2006. RG2003.

[101] F. Delay, G. Porel, and P. Sardini. Modelling diffusion in a heterogeneous rock matrix with a time-domain Lagrangian method and an inversion procedure. *C. R. Geosci.*, 334(13):967–973, 2002.

[102] F. Delay and G. Porel. Inverse modeling in the time domain for solving diffusion in a heterogeneous rock matrix. *Geophys. Res. Lett.*, 30:1147–1150, 2003.

[103] J.F. McCarthy. Continuous-time random walks on random media. *J. Phys. A-Math. Gen.*, 26:2495–2503, 1993.

[104] P. Sardini, F. Delay, K.-H. Hellmuth, G. Porel, and E. Oila. Interpretation of out-diffusion experiments on crystalline rocks using random walk modeling. *J. Cont. Hydrol.*, 61(1-4):339–350, 2003.

[105] P. Sardini, J.C. Robinet, M. Siitari-Kauppi, F. Delay, and K.-H. Hellmuth. Direct simulation of heterogeneous diffusion and inversion procedure applied to an out-diffusion experiment. Test case of Palmottu granite. *J. Cont. Hydrol.*, 93(1-4):21–37, 2007.

[106] J.C. Robinet, P. Sardini, D. Coelho, J.C. Parneix, D. Prêt, S. Sammartino, E. Boller, and S. Altmann. Effects of mineral distribution at mesoscopic scale on solute diffusion in a clay-rich rock: Example of the Callovo-Oxfordian mudstone (Bure, France). *Water Resour. Res.*, 48, 2012. W05554.

[107] A. Lindberg and M. Paananen. Petrography, lithogeochemistry and petrophysics of rock samples from Konginkangas, Sievi and Eurajoki study sites, southern and western Finland. drill holes KI-KR7, SY-KR7 and OL-KR6. Technical Report 92-34, TVO, 1992. in Finnish.

[108] P. P. Anttila, Kuivamäki. A., A. Lindberg, M. Kurimo, and M. Paananen. Geology of the Syyry area. Summary Report. Tecnical Report YJT-93-19, Imatran voima, 1993.

[109] P. Hölttä, M. Siitari-Kauppi, A. Lindberg, and A. Hautojärvi. Na, Ca, and Sr retardation on crushed crystalline rock. *Radiochim. Acta*, 82:279–285, 1998.

[110] A. Lindberg and M. Siitari-Kauppi. Shear-zone-related hydrothermal alteration in Proterozoic rocks in Finland. In G.B. Arehart and J.R. Hulston, editors, *Water-Rock Interaction - WRI-9*, pages 413–416, Rotterdam, 1998. IAGC.

[111] H.S. Carslaw and J.C. Jaeger. *Conduction of heat in solids*. Clarendon Press, Oxford, 1965.

[112] N. Perez. *Electrochemistry and corrosion science*. Kluwer Academic Publishers, Boston, 2004.

[113] V.M.M. Lobo, A.C.F. Ribeiro, and L.M.P. Verissimo. Diffusion coefficients in aqueous solutions on potassium chloride at high and low concentrations. *J. Mol. Liq.*, 78(1-2):139–149, 1998.

[114] M. Sahimi. Flow phenomena in rocks: From continuum models to fractals, percolation, cellular automata, and simulated annealing. *Rev. Mod. Phys.*, 65(4):1393–1534, 1993.

[115] A.C: Kak and M. Slaney. *Principles of computerized tomographic imaging*. IEEE Press, New York, 1988.

[116] S.R. Stock. *Microcomputed tomography: Methodology and applications*. CRC Press, Boca Raton, 2008.

[117] G.T. Herman. *Fundamentals of computerized tomography: Image reconstruction from projections*. Springer-Verlag, London, 2009.

[118] A.M. Petrovic, J.E. Siebert, and P. E. Rieke. Soil bulk density analysis in three dimensions by computed tomographic scanning. *Soil Sci. Soc. Am. J.*, 46(3):445–450, 1982.

[119] C.L. Amos, T.F. Sutherland, B. Radzijewski, and M. Doucette. A rapid technique to determine bulk density of fine-grained sediments by X-ray computed tomography. *J. Sediment. Res.*, 66(5):1023–1024, 1996.

[120] C. Denison and W. D. Carlson. Three-dimensional quantitative textural analysis of metamorphic rocks using high-resolution computed X-ray tomography: Part I. Methods and techniques. *J. Metamorph. Geol.*, 15(1):29–44, 1997.

[121] L. A. Feldkamp, L.C. Davis, and J.W. Kress. Practical cone-beam algorithm. *J. Opt. Soc. Am. A*, 1(6):612–619, 1984.

[122] R. Gonzalez and R. Woods. *Digital image processing*. Prentice-Hall, New Jersey, 2002.

[123] S.F. Edwards and D.R. Wilkinson. The surface statistics of a granular aggregate. *Proc. R. Soc. A*, 381:17–31, 1982.

[124] F. Meyer. Topographic distance and watershed lines. *Signal Process.*, 38(1):113–125, 1994.

[125] D. J. Graham, S.P. Rice, and I. Reid. A transferable method for the automated grain sizing of river gravels. *Water Resour. Res.*, 41, 2005. W07020.

[126] M. Faessel and D. Jeulin. Segmentation of 3D microtomographic images of granular materials with the stochastic watershed. *J. Microsc.*, 239(1):17–31, 2010.

[127] M. Stickler and G. Meyerhoff. The spontaneous thermal polymerization of methyl-methacrylate: 5. Experimental study and computer simulation of the high conversion reaction at 130 °C. *Polymer*, 22(7):928–933, 1981.

[128] J. Lingnau and G. Meyerhoff. The spontaneous polymerization of methyl-methacrylate: 6. Polymerization in solution: participation of transfer agents in the initiation reaction. *Polymer*, 24(11):1473–1478, 1983.

[129] J. Sammaljärvi, L. Jokelainen, J. Ikonen, and M. Siitari-Kauppi. Free radical polymerisation of MMA with thermal initiator in brick and Grimsel granodiorite. *Eng. Geol.*, 135-136:52–59, 2012.

[130] S. Sammartino, M. Siitari-Kauppi, A. Meunier, P. Sardini, A. Bouchet, and E. Tevissen. An imaging method for the porosity of sedimentary rocks: Adjustment of the PMMA method - example of a characterization of a calcareous shale. *J. Sediment. Research*, 72(6):937–943, 2002.

[131] P. Sardini, E. Moreau, S. Sammartino, and G. Touchard. Primary minerals connectivity of polyphasic igneous rocks by high-quality digitalisation and 2D image analysis. *Comput. Geosci.*, 25(5):599–608, 1999.

[132] C.S. Hutchison. *Laboratory handbook of petrolographic techniques.* Wiley & Sons, New York, 1974.

[133] J. MacQueen. Some methods for classification and analysis of multivariate observations. In L. M. Le Cam and J. Neyman, editors, *Proceedings of the Fifth Berkeley Symposium on Mathematical Statistics and Probability*, pages 281–297, Berkeley, 1967. University of California Press.

[134] G.B. Coleman and H.C. Andrews. Image segmentation by clustering. *"Proc. IEEE"*, 67(5):773–785, 1979.

[135] S.P. Lloyd. Least squares quantization in pcm. *IEEE T. Inform. Theory*, 28(2):129–136, 1982.

[136] D. A. Forsyth and J. Ponce. *Computer vision: A modern approach*. Prentice-Hall, New Jersey, 2002.

[137] P.S. Bradley and U.M. Fayyad. Refining initial points for k-means clustering. In J. Shavlik, editor, *Proceedings of the 15th International Conference on Machine Learning*, pages 91–99, San Francisco, 1998. Morgan kaufmann.

[138] S.S. Khan and A. Ahmad. Cluster center initialization algorithm for k-means clustering. *Pattern Recogn. Lett.*, 25(11):1293–1302, 2004.

[139] M.J. Li, M.K. Ng, Y.-M. Cheung, and J.Z. Huang. Agglomerative fuzzy k-means clustering algorithm with selection of number of clusters. *IEEE T. Knowl. Data En.*, 20(11):1519–1534, 2008.

[140] G.S Koch and R.F. Link. *Statistical analysis of geological data*. Dover Publications, New York, 2002.

[141] R. Mills. Self-diffusion in normal and heavy water in the range 1-45°. *J. Physical Chem.*, 77(5):685–688, 1973.

[142] J.R. Hunter, P.D. Craig, and H.E Phillips. On the use of random walk models with spatially variable diffusivity. *J. Comput. Phys.*, 106(2):366–376, 1993.